The Astronomical Journal, 158:169 (27pp), 2019 October https://doi.org/10.3847/1538-3881/ab3e72

The Hot Gas Exhaust of Starburst Engines in Mergers: Testing Models of Stellar Feedback and Star Formation Regulation

Beverly J. Smith[1], Peter Wagstaff[1], Curtis Struck[2], Roberto Soria[3,4], Brianne Dunn[1,5], Douglas Swartz[6], and Mark L. Giroux[1]

[1] Department of Physics and Astronomy, East Tennessee State University, Johnson City, TN 37614, USA
[2] Department of Physics and Astronomy, Iowa State University, Ames, IA 50011, USA
[3] College of Astronomy and Space Sciences, University of the Chinese Academy of Sciences, Beijing 100049, People's Republic of China
[4] Sydney Institute for Astronomy, School of Physics A28, The University of Sydney, Sydney, NSW 2006, Australia
[5] Now at Department of Physics and Astronomy, Clemson University, Clemson, SC 29634, USA
[6] Astrophysics Office, NASA Marshall Space Flight Center, ZP12, Huntsville, AL 35812, USA
Received 2019 June 14; revised 2019 August 6; accepted 2019 August 25; published 2019 September 30

Abstract

Using archival data from the *Chandra X-ray telescope*, we have measured the spatial extent of the hot interstellar gas in a sample of 49 nearby interacting galaxy pairs, mergers, and merger remnants. For systems with SFR $> 1\ M_{\odot}\ \mathrm{yr}^{-1}$, the volume and mass of hot gas are strongly and linearly correlated with the star formation rate (SFR). This supports the idea that stellar/supernovae feedback dominates the production of hot gas in these galaxies. We compared the mass of X-ray-emitting hot gas M_{X}(gas) with the molecular and atomic hydrogen interstellar gas masses in these galaxies ($M_{\mathrm{H_2}}$ and $M_{\mathrm{H\ I}}$, respectively), using published carbon monoxide and 21 cm H I measurements. Systems with higher SFRs have larger $M_{\mathrm{X}}(\mathrm{gas})/(M_{\mathrm{H_2}} + M_{\mathrm{H\ I}})$ ratios on average, in agreement with recent numerical simulations of star formation and feedback in merging galaxies. The $M_{\mathrm{X}}(\mathrm{gas})/(M_{\mathrm{H_2}} + M_{\mathrm{H\ I}})$ ratio also increases with dust temperature on average. The ratio $M_{\mathrm{X}}(\mathrm{gas})/\mathrm{SFR}$ is anticorrelated with the *Infrared Astronomical Satellite* 60–100 μm flux ratio and with the *Spitzer* 3.6–24 μm color. These trends may be due to variations in the spatial density of young stars, the stellar age, the ratio of young to old stars, the initial mass function, and/or the efficiency of stellar feedback. Galaxies with low SFR ($<1\ M_{\odot}\ \mathrm{yr}^{-1}$) and high K band luminosities may have an excess of hot gas relative to the relation for higher SFR galaxies, while galaxies with low K band luminosities (and therefore low stellar masses) may have a deficiency in hot gas, but our sample is not large enough for strong statistical significance.

Key words: galaxies: interactions – galaxies: ISM – X-rays: galaxies

1. Introduction

Feedback from stellar winds, radiation pressure, and supernovae play a major role in regulating star formation, by heating, ionizing, and accelerating the interstellar gas and adding turbulence. However, the details of these processes are not well-understood. Computer simulations are frequently used to study stellar feedback and star formation, using various prescriptions to model the feedback. These processes are complicated to model, because different feedback mechanisms help regulate star formation in different ways, multiple mechanisms operate simultaneously, and the different mechanisms affect each other. Radiation pressure from young stars disrupts molecular clouds, decreasing the amount of dense gas and preventing overly rapid gravitational collapse of clouds (Hopkins et al. 2011, 2013b, 2014), while shock heating by supernovae and stellar winds is responsible for most of the hot X-ray-emitting gas in galaxies (Hopkins et al. 2012b). Before supernovae begin in a young star-forming region, radiation pressure and stellar winds clear out dense gas in star-forming regions, heating and stirring the gas; later supernovae thus occur in lower-density gas, causing the hot gas to survive longer and inhibiting subsequent star formation (Hopkins et al. 2012a; Agertz et al. 2013). The more efficient the feedback, the lower the efficiency of subsequent star formation (Cox et al. 2006; Hopkins et al. 2013b). Supernovae provide both thermal energy, heating the gas, as well as kinetic feedback, which increases turbulence and thus affects later star formation (Springel 2000; Hopkins et al. 2014). Another way feedback regulates star formation is by removing gas from the main disk of the galaxy, either temporarily or permanently (e.g., Muratov et al. 2015). Supernova-driven winds may drive gas out into the halo; this hot halo material may then cool and fall back in on the galaxy, triggering delayed star formation (Hopkins et al. 2013a). Winds due to supernovae may remove gas from the galaxy entirely; in some simulations, the mass loss rate from supernovae-driven winds is greater than the star formation rate (SFR) (Hopkins et al. 2012a, 2013a).

The latest generation of simulations include multiphase interstellar gas, in order to follow the dense cores of molecular clouds where star formation occurs, the warmer atomic gas, and the hot intracloud medium (Hopkins et al. 2013b, 2014; Renaud et al. 2013, 2014, 2015, 2019; Sparre & Springel 2016a; Fensch et al. 2017; Moreno et al. 2019). The results of such simulations sometimes depend upon the resolution of the simulation and the details of the calculations, with higher-resolution models producing more efficient star formation (Teyssier et al. 2010; Hopkins et al. 2013a; Hayward et al. 2014; Sparre & Springel 2016a), and the duration and intensity of a starburst depending upon the prescription for feedback assumed in the model (Hopkins et al. 2012a; Fensch et al. 2017). How stellar feedback is implemented in these codes has profound cosmological consequences. Stellar feedback is needed in cosmological simulations of galaxy formation and evolution to explain the observed galaxy mass function (Kereš et al. 2009), the galaxy stellar mass–halo mass relation (Hopkins et al. 2014; Agertz & Kravtsov 2015, 2016;

Trujillo-Gomez et al. 2015) and the galaxian mass–metallicity relation (Finlator & Davé 2008; Ma et al. 2016; Torrey et al. 2019). For cosmological models to reproduce the so-called galaxy main sequence (a correlation between stellar mass and star formation; see Brinchmann et al. (2004), Noeske et al. (2007) and Salim et al. (2007)) or the Kennicutt-Schmidt Law (a relation between SFR and molecular gas mass; see Schmidt (1959), Kennicutt (1998), and Kennicutt & Evans (2012)), stellar feedback is necessary (Hopkins et al. 2014; Orr et al. 2018).

To test these feedback models, X-ray observations are required. With high-resolution X-ray imaging, the distribution, temperature, and mass of the hot gas within galaxies can be studied and compared to other properties of the galaxies. In star-forming galaxies, the bulk of the hot gas is attributed to feedback from SN II and young stars (Strickland et al. 2000, 2004a, 2004b; Grimes et al. 2005; Owen & Warwick 2009; Mineo et al. 2012b; Li & Wang 2013; Smith et al. 2018). Hopkins et al. (2012a) model the X-ray production due to stellar feedback in different types of galaxies. They conclude that, for normal spirals and dwarf galaxies, supernovae and stellar winds dominate, but in intense starbursts, radiation pressure dominates. The soft X-rays from galactic winds originate from a small fraction of the total hot gas; the bulk of the hot gas has such low density that it is difficult to observe directly (Strickland & Stevens 2000). Freely flowing hot gas produces little X-ray emission, in contrast to hot gas confined by surrounding cooler gas (Hopkins et al. 2012a). Observational studies show that, for star-forming galaxies, the X-ray luminosity from hot gas, L_X(gas), is proportional to the SFR (Strickland et al. 2004b; Grimes et al. 2005; Mineo et al. 2012b; Smith et al. 2018). This is in contrast to some theoretical estimates, which predict that L_X(gas) should be proportional to SFR^2 (Chevalier & Clegg 1985; Zhang et al. 2014). More modern theoretical calculations including gravitational forces and improved radiative cooling are able to reproduce the observed L_X(gas) $\propto$ SFR relation for star-forming galaxies if the mass-loading factor (mass outflow rate/SFR) decreases as SFR increases (Bustard et al. 2016; Meiksin 2016). The recent cosmological hydrodynamical simulations of van de Voort et al. (2016), which include feedback, find a constant L_X(gas)/SFR ratio for galaxies with halo masses between $10^{10.5}$ and 10^{12} $M_\odot$, where the Milky Way has a halo mass of $\sim 10^{12}$ $M_\odot$.

Over timescales of many gigayears, virialization of gas provided by stellar mass loss from older stars can contribute to the X-ray-emitting hot gas in galaxies, particularly in massive galaxies with low SFRs (e.g., Ciotti et al. 1991; Pellegrini & Ciotti 1998; Mathews & Brighenti 2003). This contribution dominates in quiescent early-type galaxies, as L_X(gas) increases with mass rather than with SFR (e.g., O'Sullivan et al. 2001; Kim & Fabbiano 2013; Su et al. 2015; Goulding et al. 2016). The possible existence of this additional source of hot gas may need to be taken into account when interpreting X-ray data in terms of stellar feedback, particularly in galaxies with low SFRs and high masses.

In the current study, our goal is to track the evolution of the hot gas in galaxies compared to the other components of the galaxies, particularly the molecular and atomic gas, and draw further comparisons with expectations from theoretical models. This study is a follow-up to our earlier archival *Chandra* study of 49 nearby major mergers in a range of merger stages (Smith et al. 2018, hereafter Paper I). In the earlier study, we removed the resolved point sources and extracted the spectrum of the diffuse X-ray emission. We then separated this spectrum into a power law and a thermal component, and corrected for internal absorption. Assuming the thermal component was due to hot gas, we compared the thermal luminosity L_X(gas) with the global SFR as derived from UV/optical data. Although there is considerable system-to-system variation in the L_X(gas)/SFR ratio, we did not see any trends of L_X(gas)/SFR with merger stage, active galactic nuclei (AGN) activity, or SFR for galaxies with SFR > 1 $M_\odot$ yr^{-1}. These results suggest that, in star-forming galaxies, stellar feedback reaches an approximately steady-stage condition. In Paper I, we concluded that, for star-forming galaxies, about 2% of the total energy output from supernovae and stellar winds is converted into X-ray flux; this result is in agreement with earlier results from smaller samples of galaxies (Grimes et al. 2005; Mineo et al. 2012b).

In the current study, we revisit the same sample of mergers and use the *Chandra* data to derive the spatial extent of the hot gas in these galaxies—and therefore the mass of hot X-ray-emitting gas M_X(gas). We compare M_X(gas) with the amount of cold molecular and atomic hydrogen gas in these galaxies, as obtained from published carbon monoxide and 21 cm H I observations. Our goal is to better understand how interstellar gas cycles between hot and cold phases due to star formation and stellar feedback, and how this cycle affects the efficiency of star formation (SFE).

In Section 2 of this paper, we review the selection of the sample and the available ultraviolet, infrared, and optical data. In Section 3, we explain the molecular and atomic hydrogen gas data. In Section 4, we determine the spatial extent of the hot gas in the galaxies. We obtain the volume and mass of hot X-ray-emitting gas and the electron density in Section 5. These values are then compared with other parameters of the systems in Section 6. The results are discussed in Section 7, and conclusions are provided in Section 8.

2. Sample Selection and UV/IR/Optical Data

The sample selection is described in detail in Paper I. Briefly, the sample includes 49 premerger interacting pairs, postmerger remnants, and midmerger systems in the nearby universe (distance $<$180 Mpc). Initially, galaxies were chosen based on their morphologies from the Arp (1966) Atlas of Peculiar Galaxies, or from other published surveys of mergers and merger remnants, selecting approximately equal-mass interacting pairs or the remnants of the merger of such pairs. The final sample was then selected based on the availability of suitable *Chandra* data. See Paper I for details.

The sample of galaxies is given in Table 1. Table 1 also provides basic data on these systems from Paper I, including distances assuming a Hubble constant of 73 km s^{-1} Mpc^{-1}, correcting for peculiar velocities due to the Virgo Cluster, the Great Attractor, and the Shapley Supercluster. The median distance for our sample galaxies is 51.5 Mpc. Table 1 also provides the far-infrared luminosity L_{FIR} and the near-infrared K band luminosity L_K, obtained from *Infrared Astronomical Satellite* (*IRAS*) and Two Micron All-Sky Survey (2MASS) data, respectively, as described in Paper I. In addition, Table 1 includes SFRs, derived from a combination of *Spitzer* infrared and *GALEX* UV photometry as described in Paper I. When available, the far-UV is used; otherwise, near-UV (NUV) photometry is used. These SFRs correspond to the SFR

Table 1
Basic Data on Sample Galaxies

Name	Stage	Distance (Mpc)	log L_{FIR} ($L_\odot$)	log L_K ($L_\odot$)	SFR ($M_\odot$ yr^{-1})	log L_X(gas) (erg s^{-1})	AGN?
AM 1146-270	6	24.6	8.98	9.49	0.23	38.91	
AM 2055-425	5	179.1	11.72	11.27	128.23	41.92	
Arp 091	1	34	10.33	10.93	4.22	40.72	Sy2
Arp 147	1	129	10.22	10.80	3.65	40.76	
Arp 148	1	146.9	11.38	11.14	14.40	41.28	
Arp 155	7	46	9.99	10.98	1.00	40.01	
Arp 157	4	30.5	10.69	10.99	5.61	40.25	
Arp 160	5	39	10.72	10.70	15.14	41.15	
Arp 163	7	23.1	9.39	9.93	1.19	<39.57	
Arp 178	5	62.1	10.11	11.54	1.92	40.59	
Arp 186	5	64.2	11.27	11.20	60.33	41.34	Sy2:HII
Arp 217	6	18.0	10.24	10.43	7.13	40.6	
Arp 220	4	83	12.03	11.27	95.65	41.34	Sy
Arp 222	6	26.1	8.71	11.12	0.27	39.85	
Arp 226	5	67	10.48	11.30	4.52	40.89	
Arp 233	7	25	9.62	9.99	1.57	39.73	
Arp 235	7	13	8.75	9.42	0.03	<39.3	
Arp 236	1	81	11.39	11.18	51.02	41.88	
Arp 240	2	102	11.29	11.68	36.18	41.26	
Arp 242	2	98	10.65	11.20	6.23	40.78	
Arp 243	5	79.4	11.34	11.00	21.68	<40.41	
Arp 244	3	24.1	10.62	11.26	9.70	40.67	
Arp 256	2	109.6	11.13	11.13	35.75	41.17	
Arp 259	2	55	10.34	10.20	6.20	40.42	
Arp 261	1	29	9.26	9.66	0.62	39.22	
Arp 263	5	9.8	8.76	9.06	0.22	<38.76	
Arp 270	1	29	10.16	10.65	4.93	40.17	
Arp 283	1	30	10.48	10.77	5.74	40.46	
Arp 284	2	39	10.41	10.68	9.31	40.81	
Arp 293	2	82	11.10	11.41	12.24	41.54	LINER/H II
Arp 295	2	94	10.86	11.50	9.29	41.11	
Arp 299	3	48	11.60	11.37	119.01	41.51	
IRAS 17208-0014	6	183	12.19	11.40	133.97	42.03	LINER
IRAS 23128-5919	3	184	11.71	11.24	133.83	41.79	
Mrk 231	5	178.1	12.13	12.36	450.05	41.39	Sy1
Mrk 273	4	160.5	11.90	11.44	116.83	41.19	Sy2
NGC 034	5	79.3	11.18	11.14	30.78	41.09	Sy2
NGC 1700	7	52.5	8.40	11.57	0.24	40.75	
NGC 2207/IC 2163	3	38.0	10.73	11.48	9.03	40.76	
NGC 2865	7	37.9	9.53	11.14	0.10	39.75	
NGC 3256	4	37.0	11.30	11.26	38.50	41.35	
NGC 3353	6	18.5	9.43	9.66	0.91	39.19	
NGC 5018	7	38.4	9.40	11.44	0.39	40.58	
NGC 5256	3	120.9	11.21	11.62	32.02	41.35	Sy2
NGC 6240	4	108.8	11.61	11.81	88.46	42.08	Sy2/LINER
NGC 7592	3	99.5	11.08	11.07	26.08	41.22	Sy2
UGC 2238	5	87.1	11.04	11.15	9.41	40.97	LINER
UGC 5101	5	164.3	11.72	11.51	115.63	41.56	Sy1
UGC 5189	2	48.9	9.48	9.47	1.54	<39.26	

averaged over a time period of ∼100 Myr (Kennicutt & Evans 2012). Table 1 also identifies the 13 galaxies in the sample that are classified in the NASA Extragalactic Database (NED[7]) as Seyfert 1, Seyfert 2, or low-ionization nuclear emission-line region (LINER) galaxies. Detailed descriptions of the individual galaxies in the sample are provided in the Appendix of Paper I.

In Paper I, we classified the systems into seven merger stages based on their morphologies. These stages are: (1) separated but interacting pair with small or no tails; (2) separated pair with moderate or long tails; (3) pair with disks in contact; (4) common envelope, two nuclei, and tails; (5) single nucleus and two strong tails; (6) single nucleus but weak tails; and (7) disturbed elliptical with small or no tails. The staging is approximate, with an uncertainty of ±1 stage.

In Figure 1, various properties of the galaxies (distance, L_{FIR}, the L_{FIR}/L_K ratio, and the *IRAS* 60–100 μm flux ratio F_{60}/F_{100}) are plotted against the merger stage. The black open squares in Figure 1 are the data for the individual galaxies; the blue filled diamonds that are offset slightly to the left of the stage show

[7] http://ned.ipac.caltech.edu

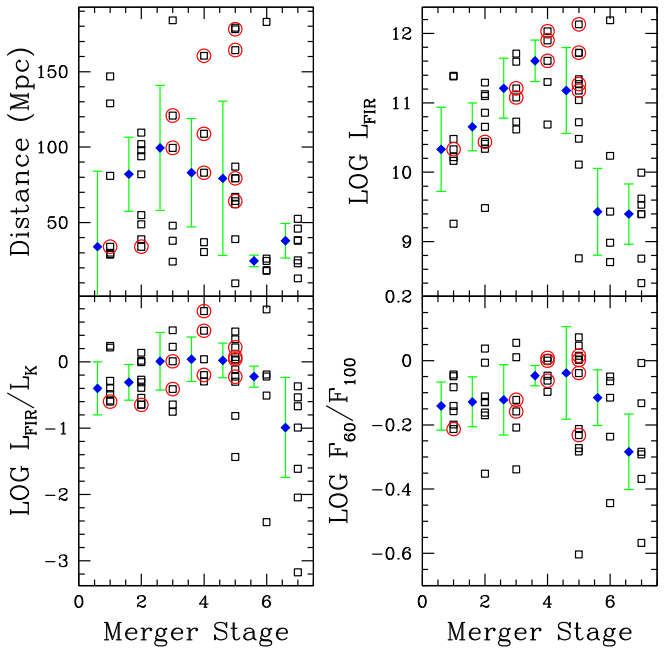

Figure 1. Plots of basic galaxy properties (distance, $L_{\rm FIR}$, $L_{\rm FIR}/L_{\rm K}$, and F_{60}/F_{100}) vs. merger stage. Black open squares mark the sample galaxies, with those circled by red circles being AGN. The filled blue diamonds are the median values for each stage, slightly offset to the left. The error bars plotted on the median values display the semi-interquartile range, equal to half the difference between the 75th percentile and the 25th percentile.

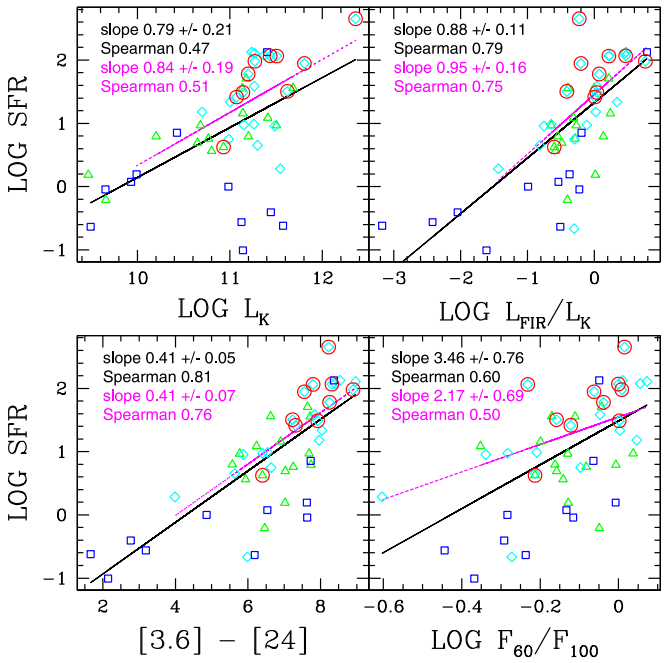

Figure 2. Correlations between basic galaxy properties (SFR vs. $L_{\rm K}$, $L_{\rm FIR}/L_{\rm K}$, [3.6]–[24], and F_{60}/F_{100}). The best-fit line for the full sample is plotted as a solid black line, while the best-fit line for systems with SFR $> 1.0\,M_{\odot}\,{\rm yr}^{-1}$ is given as a dotted line. The best-fit slope and the Spearman rank correlation coefficient for the full set are shown in black (on top), while the values for the high-SFR subset are shown in magenta (below). Systems at merger stages 1 and 2 are marked as open green triangles. Merger stages 3, 4, and 5 are indicated by open cyan diamonds. Merger stages 6 and 7 are identified by blue open squares. AGN are identified by red circles.

the median value for that stage. The error bars on the blue diamonds show the semi-interquartile range, equal to half the difference between the 75th percentile and the 25th percentile. As discussed in Paper I, this sample is inhomogeneous because it was selected based on the availability of archival *Chandra* data. As illustrated in Figure 1, the sample has some biases. The galaxies in the middle of the merger sequence tend to be more distant, and so tend to have higher FIR luminosities. This means they have higher SFRs, because $L_{\rm FIR}$ is an approximate measure of the SFR for galaxies with high SFRs (e.g., Kennicutt 1998; Kennicutt & Evans 2012). The late-stage mergers tend to be closer and have lower $L_{\rm FIR}$. Late-stage mergers are difficult to identify at large distances, and thus confirmed examples tend to be nearby.

The late-stage mergers also tend to have lower $L_{\rm FIR}/L_{\rm K}$ ratios. This ratio is an approximate measure of the specific SFR (sSFR), defined as the SFR/stellar mass, because the K band luminosity $L_{\rm K}$ is an approximate measure of the stellar mass (Maraston 1998; Bell & de Jong 2000; Into & Portinari 2013; Andreani et al. 2018), although it is affected by age and possible AGN contributions. The midmerger systems also tend to have higher dust temperatures, as traced by the *IRAS* F_{60}/F_{100} ratio (last panel Figure 1). The uncertainty in the staging, the biases in the sample, and the small number of systems in each stage mean that trends with merger stage are uncertain. As seen in Figure 1, the AGN tend to be midmerger systems with high $L_{\rm FIR}$ and F_{60}/F_{100}. Although AGN can contribute to the heating of interstellar dust in galaxies, for most of our AGN, published studies of the IR spectra of the galaxies conclude that dust heating is dominated by star formation rather than the AGN (see the detailed discussions on the individual galaxies in the Appendix of Paper I).

Figure 2 displays some well-known correlations between these basic parameters. The observed correlation between SFR and $L_{\rm K}$ (top left panel) or its equivalent has been seen many times before for star-forming galaxies (e.g., Smith et al. 1996; Andreani et al. 2018). This relation is a consequence of the correlation between SFR and stellar mass, which is known as the "galaxy main sequence" for star-forming galaxies (e.g., Brinchmann et al. 2004; Salim et al. 2007). For our sample, this correlation is only a weak correlation, because of the inclusion of some systems with low SFRs compared to $L_{\rm K}$. Galaxies with low SFR compared to the best-fit "galaxy main sequence" relation are considered quenched, quenching, or post-starburst galaxies. In our sample, our post-starburst galaxies are all late-stage mergers and have low $L_{\rm FIR}/L_{\rm K}$ ratios.

Figure 2 shows that the SFR is correlated with both $L_{\rm FIR}/L_{\rm K}$ and the *Spitzer* [3.6 μm]–[24 μm] color for our sample galaxies.[8] The majority of our galaxies fall in a narrow range of $L_{\rm FIR}/L_{\rm K}$, $-1 \leqslant \log\, L_{\rm FIR}/L_{\rm K} \leqslant 0$, but a handful have lower $L_{\rm FIR}/L_{\rm K}$ ratios (the post-starburst systems with low SFRs) and a few have higher $L_{\rm FIR}/L_{\rm K}$ ratios. The [3.6]–[24] color is an approximate measure of the ratio of the number of young-to-old stars (e.g., Smith et al. 2007), increasing with increasing proportions of young stars. This means that [3.6]–[24] is another approximate measure of the sSFR.

Figure 2 also shows that F_{60}/F_{100} is weakly correlated with SFR, with considerable scatter. This relation or its equivalent has been noted before (e.g., Smith et al. 1987; Soifer et al. 1987). Higher F_{60}/F_{100} ratios imply hotter dust on average and more intense UV interstellar radiation fields (ISRF) (e.g.,

[8] Here, [3.6]–[24] is defined as the magnitude in the 3.6 μm filter minus that in the 24 μm filter, using zero magnitude flux densities of 277.5 Jy and 7.3 Jy, respectively.

Desert et al. 1990), which are correlated but not perfectly with the overall SFR of the galaxy.

3. Atomic and Molecular Interstellar Gas

In the current study, we compare the hot X-ray-emitting gas mass in these galaxies with the interstellar molecular and atomic hydrogen gas masses. We obtained published measurements of the 2.6 mm CO (1–0) fluxes of the sample galaxies from the literature, and used these to derive molecular gas masses. As there is some uncertainty as to the relation between the CO luminosity and the molecular gas mass, we converted the CO fluxes into molecular gas masses M_{H_2} via two methods. First, we calculated M_{H_2} for all galaxies, assuming a constant conversion equal to the Galactic conversion factor between H_2 column density $N(H_2)(cm^{-2})$ and CO intensity $I(CO)$ of $N(H_2)(cm^{-2}) = 2.0 \times 10^{20}$ I(CO)(K km s^{-1}) (Dame et al. 2001; Bolatto et al. 2013). The Galactic conversion is thought to be appropriate for most galaxies, but low-metallicity systems may be deficient in CO relative to H_2, while extreme starburst galaxies may have enhanced CO/H_2 ratios (e.g., Downes & Solomon 1998; Bolatto et al. 2013). Thus, for comparison, we made a second estimate of M_{H_2}, using a variable CO/H_2 ratio. For galaxies with $L_{FIR} > 10^{11} L_\odot$ (e.g., extreme starbursts), we used a lower conversion factor of 4×10^{19} cm^{-2}/(K km s^{-1}) (e.g., Ueda et al. 2014). For galaxies with low K band luminosities (e.g., possible low-metallicity systems), $L_K < 10^{10} L_\odot$, we used an enhanced ratio of 5×10^{20} cm^{-2}/(K km s^{-1}) (e.g., Bolatto et al. 2013). For all other galaxies, we used the standard Galactic value given above. Because accurate metallicities are not available for all of the galaxies in our sample and there is some uncertainty as to how the CO/H_2 ratio varies with metallicity, we do not use a more complicated metallicity-dependent conversion in this study. In Section 6 of this paper, we compare various properties of the galaxies. We do the correlation analysis with both CO/H_2 ratios, to test whether our conclusions are influenced by our choice of CO/H_2 conversion factors.

Molecular gas masses calculated with a constant CO/H_2 ratio equal to the Galactic value are provided in column 2 of Table 2. Molecular gas masses calculated with the variable CO/H_2 ratio are given in column 3 of Table 2. The reference for the original CO measurement is given in column 4 of Table 2. Note that molecular masses are not available for all of the galaxies in the sample. In some cases, no CO observations have been published. In other cases, only measurements of the central region have been made, where the beam size is significantly smaller than the optical extent of the galaxy. In those cases, we are not able to get reliable upper limits to the global molecular gas content, so no molecular gas mass is listed in Table 2. Follow-up CO observations would be useful to complete the molecular gas census of the sample galaxies.

In the bottom row of Figure 3, the star formation efficiency, which we define as the global SFR/M_{H_2} ratio for the galaxy,[9] is plotted against the merger stage. The left panel of Figure 3 has SFE calculated with a constant CO/H_2 ratio and the right with the variable CO/H_2 ratio. These two determinations of the SFE are included in Table 2, in columns 5 and 6, respectively. As in Figure 1, the black open squares in Figure 3 are the data for the individual galaxies; the blue filled diamonds that are offset

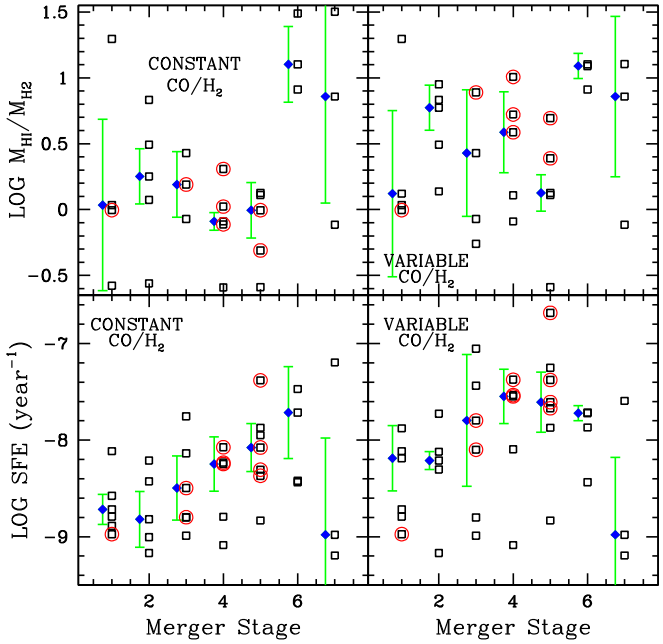

Figure 3. Top row: plots of the H I mass/H_2 mass against the merger stage. Bottom row: plots of the SFE against the merger stage. In the left panels, the standard Galactic CO/H_2 ratio is used for all galaxies. In the right panels, a variable CO/H_2 ratio is used. Black open squares mark the sample galaxies, with those circled by red circles being AGN. The filled blue diamonds are the median values for each stage, slightly offset to the left. The error bars plotted on the median values display the semi-interquartile range, equal to half the difference between the 75th percentile and the 25th percentile.

slightly to the left of the stage show the median value for that stage. The error bars on the blue diamonds show the semi-interquartile range, equal to half the difference between the 75th percentile and the 25th percentile.

Systems in the middle merger stages tend to have higher SFEs than those in the early stages. This is consistent with earlier surveys that found L_{FIR}/M_{H_2} to be enhanced near nuclear coalescence (Casoli et al. 1991; Georgakakis et al. 2000). Given the small numbers of galaxies per merger stage in our sample and the spread in the data per merger stage, however, this result is uncertain for our sample, especially if one also takes into account the selection effects and the uncertainties in the CO/H_2 ratio. Because of these factors, any trends with merger stage are uncertain for our sample.

We also scoured the literature for measurements of the global H I masses of our galaxy sample. These values are tabulated in column 7 of Table 2, and the reference for the H I data is given in column 8. In Figure 3, we provide plots of merger stage versus quantities derived from the CO and H I data. The top row of Figure 3 compares $M_{H\,I}/M_{H_2}$ with the merger stage. In the left panel, we assume a constant CO/H_2 ratio in calculating M_{H_2}, while in the right panel, we use the variable CO/H_2 ratio. An apparent increase in the H I gas fraction in the late stages of the merger sequence (left panel) is weakened when a variable CO/H_2 ratio is used (right panel).

The SFE is plotted against dust temperature as measured by the *IRAS* 60–100 μm flux ratio in the two top panels of Figure 4, for the two CO/H_2 conversion factors. A trend is clearly visible, in that hotter dust is correlated with more efficient star formation. This relation is well-known (e.g., Young et al. 1986; Sanders et al. 1991). Note that the scatter is larger with the variable CO/H_2 ratio than for the constant

[9] With this definition, the SFE is equal to $1/\tau_{dep}$, where τ_{dep} is the global depletion timescale, i.e., the time to use up the molecular gas.

Table 2
Global Molecular and Atomic Gas Mass in the Sample Galaxies

Name	LOG M_{H_2}[a] ($M_\odot$)	LOG M_{H_2}[b] ($M_\odot$)	CO REF[c]	LOG SFE[a] (yr^{-1})	LOG SFE[b] (yr^{-1})	LOG $M_{H\,I}$ ($M_\odot$)	H I REF[d]	LOG M_{hot} ($M_\odot$)	LOG M_{hot}/M_{cold}[a]	LOG log M_{hot}/M_{cold}[b]
AM 1146-270						9.15	16	6.85		
AM 2055-425	10.06	9.36	1	−7.94	−7.24			9.34		
Arp 091	9.60	9.60	2	−8.96	−8.96	9.60	17	7.66	−2.23	−2.23
Arp 147	9.28	9.28	3	−8.71	−8.71			8.40		
Arp 148	10.05	9.35	4	−8.88	−8.18			8.76		
Arp 155	9.19	9.19	5	−9.18	−9.18	9.08	17	7.62	−1.81	−1.81
Arp 157	9.84	9.84	6	−9.08	−9.08	9.75	17	7.57	−2.52	−2.52
Arp 160	9.05	9.05	6	−7.86	−7.86	9.18	17	8.40	−1.01	−1.01
Arp 163						9.08	17			
Arp 178	10.17	10.17	2	−9.88	−9.88	9.58	17	8.04	−2.22	−2.22
Arp 186	9.86	9.16	4	−8.07	−7.37	9.55	18	8.30	−1.72	−1.39
Arp 217	8.57	8.57	7	−7.70	−7.70	9.67	17	7.87	−1.82	−1.82
Arp 220	10.23	9.53	4	−8.24	−7.54	10.54	17	8.90	−1.80	−1.67
Arp 222	7.87	7.87	8	−8.43	−8.43	8.79	17	7.15	−1.68	−1.68
Arp 226	9.49	9.49	8	−8.82	−8.82	9.60	18	7.83	−2.01	−2.01
Arp 233	7.39	7.79	9	−7.19	−7.58	8.89	17	6.96	−1.93	−1.95
Arp 235						8.85	17			
Arp 236	10.28	9.59	4	−8.57	−7.87	9.71	19	8.98	−1.40	−0.97
Arp 240	10.56	9.86	10	−8.99	−8.29	10.64	17	8.79	−2.11	−1.91
Arp 242	9.96	9.96	10	−9.16	−9.16	10.46	17	8.22	−2.35	−2.35
Arp 243	9.63	8.93	6	−8.28	−7.59	9.50	20			
Arp 244	9.98	9.98	10	−8.98	−8.98	9.90	21	8.41	−1.82	−1.82
Arp 256	9.98	9.28	10	−8.42	−7.72	10.23	17	8.43	−1.98	−1.84
Arp 259						10.21	17	8.00		
Arp 261						9.75	17	7.28		
Arp 263						9.25	17			
Arp 270	8.81	8.81	2	−8.10	−8.10	10.10	17	7.63	−2.49	−2.49
Arp 283	9.55	9.55	7	−8.78	−8.78	9.58	17	7.43	−2.43	−2.43
Arp 284	9.18	9.18	6	−8.20	−8.20	10.01	17	7.98	−2.08	−2.08
Arp 293	9.91	9.21	4	−8.81	−8.11	9.35	22	8.85	−1.15	−0.73
Arp 295						10.40	23	8.36		
Arp 299	10.21	9.51	10	−8.13	−7.43	9.25	17	9.09	−1.16	−0.61
IRAS 17208-0014	10.55	9.85	11	−8.41	−7.71			9.18		
IRAS 23128-5919	9.88	9.18	1	−7.74	−7.04			9.12		
Mrk 231	10.03	9.34	6	−7.37	−6.67			9.17		
Mrk 273	10.14	9.44	4	−8.06	−7.36	10.16	17	9.42	−1.03	−0.81
NGC 034	9.86	9.16	8	−8.36	−7.66	9.85	26	8.45	−1.70	−1.47
NGC 1700								8.67		
NGC 2207/IC 2163	9.76	9.76	15	−8.79	−8.79	10.19	17	8.40	−1.91	−1.91
NGC 2865	7.97	7.97	12	−8.97	−8.97	8.83	24	7.16	−1.72	−1.72
NGC 3256	10.38	9.68	8	−8.78	−8.08	9.79	25	8.61	−1.85	−1.41
NGC 3353	7.43	7.83	14	−7.46	−7.86	8.92	17	6.86	−2.06	−2.08
NGC 5018						8.82	17	7.64		
NGC 5256	10.30	9.60	13	−8.79	−8.09			9.29		
NGC 6240	10.18	9.48	6	−8.22	−7.52	10.07	17	9.75	−0.67	−0.41
NGC 7592	9.91	9.21	10	−8.49	−7.79	10.10	17	8.74	−1.57	−1.41
UGC 2238	9.97	9.27	4	−8.98	−8.28	9.98	17			
UGC 5101	10.37	9.67	4	−8.30	−7.60			9.10		
UGC 5189						10.14	17			

Notes.
[a] Assuming the standard Galactic CO/H_2 ratio. SFE in this paper is defined as SFR/M_{H_2}.
[b] Using the variable CO/H_2 ratio (see the text for details). SFE is defined as SFR/M_{H_2}.
[c] CO references: (1) Mirabel et al. 1990; (2) Zhu et al. 1999; (3) Horellou et al. 1995; (4) Larson et al. 2016; (5) Wiklind et al. 1995; (6) Sanders et al. 1991; (7) Young et al. 1996; (8) Ueda et al. 2014; (9) Israel 2005; (10) Bushouse et al. 1999; (11) Solomon et al. 1997; (12) Georgakakis et al. 2001; (13) Papadopoulos et al. 2012; (14) Sage et al. 1992; (15) Elmegreen et al. 2016.
[d] H I references: (16) Doyle et al. 2005; (17) Huchtmeier & Richter 1989; (18) Obreschkow & Rawlings 2009; (19) Martin et al. 1991; (20) Bushouse 1987; (21) Gordon et al. 2001; (22) van Driel et al. 2000; (23) Hibbard & van Gorkom 1996; (24) Cox & Sparke 2004; (25) English et al. 2003; (26) Fernández et al. 2014.

conversion factor. In the bottom two panels of Figure 4, we compare the SFE with the SFR for the two conversion factors. There is a trend, in that systems with the highest SFRs have high SFEs. However, there is also a lot of scatter, and there are some low-SFR systems with high SFE. A spread in the SFE for a given SFR has been observed before (e.g., Young et al. 1986;

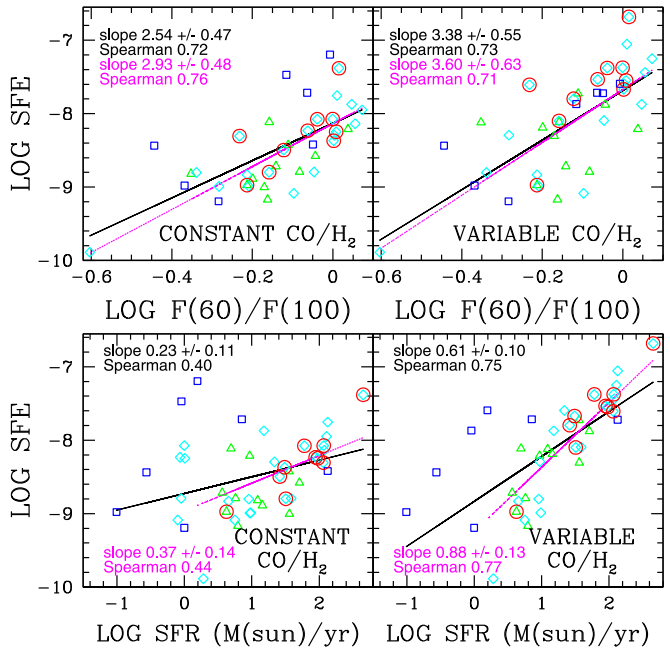

Figure 4. Comparisons between SFE and F_{60}/F_{100} (top panels) and SFE and SFR (bottom panels). The left panels use a constant CO/H_2 ratio, while the right use a variable CO/H_2 ratio. The best-fit line for the full sample is plotted as a solid black line, while the best-fit line for systems with SFR $> 1.0\,M_\odot\,yr^{-1}$ is given as a dotted line. The best-fit slope and the Spearman rank correlation coefficient for the full set are shown in black (on top), while the values for the high-SFR subset are shown in magenta (below). Systems at merger stages 1 and 2 are marked as open green triangles. Merger stages 3, 4, and 5 are indicated by open cyan diamonds. Merger stages 6 and 7 are identified by blue open squares. AGN are identified by red circles.

Sanders et al. 1991; Sanders & Mirabel 1996; Young et al. 1996; Daddi et al. 2010).

The scatter in the SFE versus SFR correlation may be due to variations in the fraction of the CO-emitting gas involved in star formation. This would lead to variations in the SFE according to our definition, SFR/M_{H_2}, where H_2 is derived from CO observations. Larger SFE may mean that a larger fraction of the CO-emitting cold molecular gas is in a dense state, an idea that is supported by both observations (Solomon et al. 1992; Gao & Solomon 2004; Juneau et al. 2009; Wu et al. 2010) and simulations (Teyssier et al. 2010; Renaud et al. 2014, 2019; Sparre & Springel 2016a). These simulations show that an increase in turbulent compression during an interaction can cause the gas probability density function to shift to higher densities, producing an increase in the amount of very high-density gas. Thus, the variations in SFE from galaxy to galaxy may be caused by differences in the dynamical state of the galaxies.

4. X-Ray Spatial Extent

All of the sample galaxies were observed with the *Chandra* ACIS-S array, and all of the galaxies fit well within the $8\farcm3 \times 8\farcm3$ field of view of the S3 chip of this array. Details of the individual observations, including exposure times and ObsID numbers, are provided in Paper I. In that work, we also identified point sources in the field using the *Chandra* Interactive Analysis of Observations (*ciao*) software tool *wavdetect*. The point sources themselves and their statistics were the subject of another paper (Smith et al. 2012).

In Paper I, after removing the point sources, we used the *ciao* software routine *specextract* to extract the diffuse X-ray spectrum within the optical *B* band 25 mag arcsec^{-2} isophote. This optical isophote was measured on Sloan Digitized Sky Survey (SDSS) g images using standard g-to-B conversion factors—or, if SDSS images were not available, equivalent levels on *GALEX* near-UV images were used; see Smith et al. (2018) for details. In Paper I, we used the *xspec*[10] software to fit the 0.3–8.0 keV background-subtracted point-source-removed spectrum within the $\mu_B = 25$ mag arcsec^{-2} isophote (e.g., D25) to a combination power-law plus thermal (MEKAL) spectrum, assuming a power-law photon index of 1.8 and correcting for both Galactic and internal absorption. The power-law component is assumed to be caused by faint unresolved point sources. The absorption-corrected 0.3–8.0 keV luminosities for the MEKAL component are provided in Table 1 of the current paper; we assume that the MEKAL component is from hot gas. These X-ray luminosities have been corrected for absorption within the galaxies as described in Paper I.

In the current study, we measured the spatial extent of the diffuse soft X-ray flux in these galaxies, and we used these estimates to calculate the electron densities and masses of the hot X-ray-emitting gas. Our procedure is as follows. After initial processing and deflaring of the data as described in Paper I, we constructed 0.3–1.0 keV maps of each galaxy. We then made an initial estimate of the spatial extent of the low energy diffuse X-ray emission by eye from the 0.3–1.0 keV maps, assuming an elliptical distribution and estimating the centroid of the emission, the radial extent, the ellipticity, and the position angle of the emission. For some of the premerger systems, two distinct regions of diffuse light are visible, associated with the two galaxies in the pair, so two elliptical regions were marked and the two regions were treated separately.

We then divided these ellipses into a set of concentric elliptical annuli, and determined background-subtracted 0.3–1.0 keV counts and photon flux surface brightness in each annulus using the *ciao* routine *dmextract*, excluding the point sources detected by the *wavdetect* software. For background subtraction, we used large areas outside of the optical extent of the galaxies excluding bright point sources. All of our target galaxies have small enough angular size(s) that we can obtain sufficient background regions on the same chip. The flux calibration was done using a 0.8 keV monoenergetic exposure map. When multiple data sets were available, each set was calibrated individually and the results combined. We then produced radial profiles for each galaxy.

The derivation of the radial profiles was done iteratively, modifying the initial region on the sky and the annuli widths until good radial profiles were produced. We started by dividing the initial preliminary ellipse into 10 radial annuli, adding three more annuli outside of the initial radius for a total of 13 annuli. If there were too few counts to get a good radial profile with 13 annuli, we divided the initial ellipse into only five annuli, and added two outside the initial region for a total of seven annuli. In some low signal-to-noise ratio (S/N) cases, obtaining sufficient counts required us to divide the initial ellipse into only three annuli, plus two additional annuli outside, for a total of five annuli. In total, we were able to

[10] https://heasarc.gsfc.nasa.gov/xanadu/xspec/

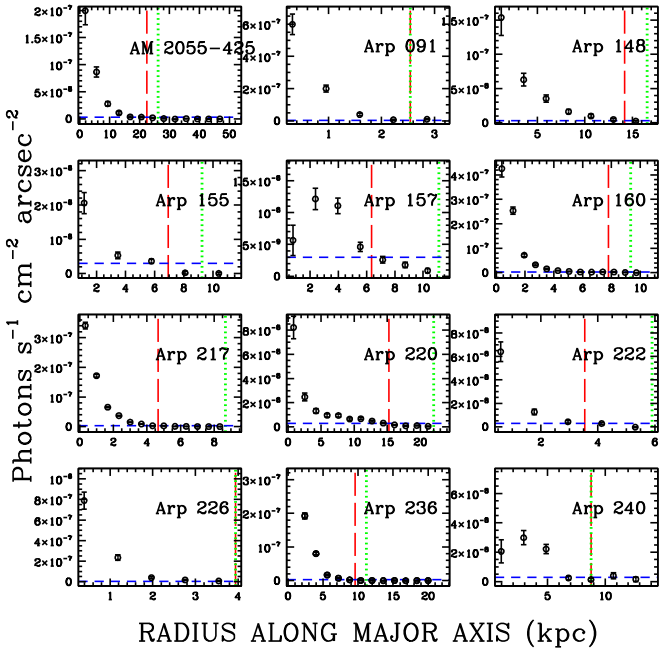

Figure 5. Montage of major axis radial profiles from elliptical annuli, plotted against the distance along the major axis. These were obtained using the *dmextract* software. The blue horizontal lines (short dashes) mark the nominal surface brightness cutoff of 3×10^{-9} photons s^{-1} cm^{-2} arcsec^{-2}. The red vertical lines (long dashes) mark the "best" estimate of the radial extent of the X-ray emission, used for the volume determination. The green vertical lines (dotted) mark the full 2σ extent, for the galaxies with high-S/N observations. See the text for more details.

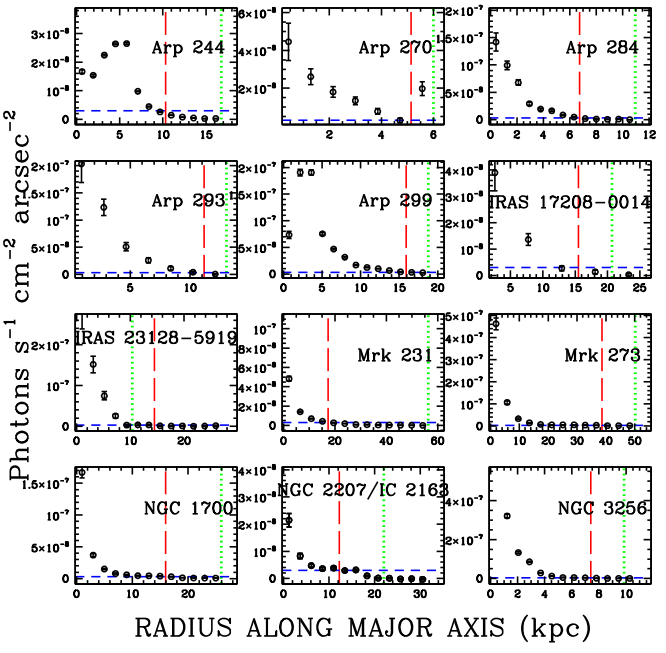

Figure 6. Montage of major axis radial profiles from elliptical annuli, plotted against the distance along the major axis. These were obtained using the *dmextract* software. The blue horizontal lines (short dashes) mark the nominal surface brightness cutoff of 3×10^{-9} photons s^{-1} cm^{-2} arcsec^{-2}. The red vertical lines (long dashes) mark the "best" estimate of the radial extent of the X-ray emission, used for the volume determination. The green vertical lines (dotted) mark the full 2σ extent, for the galaxies with high-S/N observations. See the text for more details.

derive radial profiles for 28 systems by this method, with 16 using 13 annuli, six using seven annuli, and six using five annuli.

The final background-subtracted radial profiles of the diffuse emission, as obtained from *dmextract*, are displayed in Figures 5–7, after conversion into 0.3–1.0 keV surface brightness in units of photons s^{-1} cm^{-2} arcsec^{-2}. In most cases, these radial profiles are centrally peaked, but there are a few exceptions—most notably Arp 244 and Arp 299 (see Figure 6).

As a check on these results, we also obtained radial profiles using a different method. Instead of *dmextract*, we used the *ciao* routine *specextract* to extract the soft (0.3–1.0 keV) X-ray spectra for each annulus. When multiple data sets were available, we used the "combine = yes" option, which calibrates each data set individually, then the weighted spectra were coadded. The *ISIS* (Interactive Spectral Interpretation System) software[11] (Houck & Denicola 2000) was then used to derive background-subtracted 0.3–1.0 keV counts and photon fluxes in each annuli, taking into account the calibrated response function of the detector. These two procedures give reasonably consistent radial profiles, with the *dmextract* method giving lower fluxes (by about a factor of 1.2) and somewhat smaller uncertainties. We used the *dmextract*-determined radial profiles in the subsequent determination of the radial extent of the X-ray emission in the galaxies and the following analysis.

Our goal in this paper is to obtain the physical size of the hot gas distribution within the galaxies, in order to derive electron densities and hot gas masses. One complication, however, is that how far out in the galaxy the X-ray emission can be

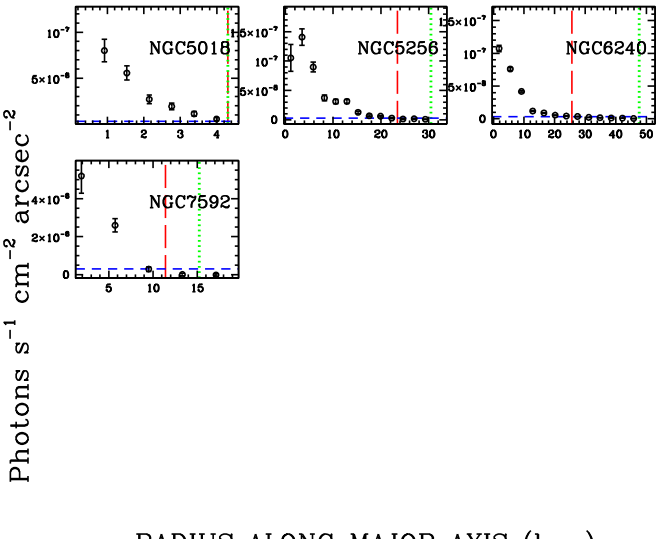

Figure 7. Montage of major axis radial profiles from elliptical annuli, plotted against the distance along the major axis. These were obtained using the *dmextract* software. The blue horizontal lines (short dashes) mark the nominal surface brightness cutoff of 3×10^{-9} photons s^{-1} cm^{-2} arcsec^{-2}. The red vertical lines (long dashes) mark the "best" estimate of the radial extent of the X-ray emission, used for the volume determination. The green vertical lines (dotted) mark the full 2σ extent, for the galaxies with high-S/N observations. See the text for more details.

detected depends upon the exposure time for the observations and the width of the annulus that is used. For the same annulus width, more sensitive observations can detect gas further out in the galaxy. This would give larger radii for the hot gas extent, although the gas in the outskirts may contribute little to the

[11] https://space.mit.edu/ASC/ISIS/

Table 3
Final Ellipses Used for Volume Calculations at 0.3–1.0 keV Surface Brightness of 3×10^{-9} photons s^{-1} cm^{-1} $arcsec^{-2}$

Name	Individual Galaxy	R.A. (J2000)	Decl. (J2000)	Major Axis Radius (″)	Minor Axis Radius (″)	Major Axis Radius (kpc)	Minor Axis Radius (kpc)	P.A.[a] (deg)	Number Annuli	Diffuse 0.3–1.0 keV Counts
AM 1146-270	ESO 504-G017	11 48 46.046	−27 22 49.11	36.″74	24.″15	4.38	2.88	0	1	27 ± 13
AM 2055-425	ESO 286-IG019	20 58 26.554	−42 38 58.11	25.″88	11.″80	22.48	10.25	65	13	289 ± 19
Arp 091	NGC 5953	15 34 32.396	+15 11 36.55	15.″42	9.″90	2.54	1.63	300	5	233 ± 17
	NGC 5954	15 34 34.911	+15 12 12.96	24.″17	11.″90	3.99	1.83	90	1	59 ± 8
Arp 147	IC 298 NED02	3 11 19.621	+1 18 51.35	8.″95	5.″40	5.60	3.38	115	1	60 ± 7
	IC 298	3 11 18.367	+1 18 57.12	15.″00	14.″40	9.38	8.77	20	1	56 ± 9
Arp 148	NED01	11 03 53.839	+40 50 58.26	19.″92	11.″51	14.19	8.20	350	7	216 ± 17
Arp 155	NGC 3656	11 23 38.541	+53 50 30.51	31.″09	15.″81	6.94	3.53	350	5	129 ± 17
Arp 157	NGC 520	1 24 34.398	+3 47 27.11	42.″92	14.″26	6.35	2.11	100	7	259 ± 19
Arp 160	NGC 4194	12 14 09.490	+54 31 32.96	41.″17	29.″27	7.79	5.54	258	13	1007 ± 35
Arp 178	NGC 5614	14 24 07.420	+34 51 32.48	23.″87	17.″33	7.19	5.22	38	1	58 ± 8
Arp 186	NGC 1614	4 34 00.068	−8 34 44.83	18.″17	11.″25	5.66	3.50	195	1	122 ± 12
Arp 217	NGC 3310	10 38 45.964	+53 30 08.73	53.″48	48.″04	4.67	4.19	230	13	4924 ± 73
Arp 220	IC 4553	15 34 57.578	+23 30 06.07	37.″87	26.″55	15.25	10.69	15	13	711 ± 32
Arp 222	NGC 7727	23 39 53.876	−12 17 34.61	27.″98	16.″53	3.54	2.09	40	5	143 ± 13
Arp 226	NGC 7252	22 20 44.774	−24 40 41.77	12.″13	9.″67	3.94	3.14	30	5	217 ± 16
Arp 233	UGC 05720	10 32 31.589	+54 24 05.25	20.″41	17.″20	2.48	2.09	30	1	127 ± 12
Arp 236	IC 1623	01 07 46.897	−17 30 26.91	24.″45	24.″37	9.60	9.57	90	13	1645 ± 42
Arp 240	NGC 5258	13 39 57.690	+0 49 56.55	24.″14	12.″50	11.94	6.18	300	1	130 ± 13
	NGC 5257	13 39 53.221	+0 50 19.82	23.″63	15.″50	11.69	7.55	25	7	127 ± 14
Arp 242	NGC 4676B	12 46 11.236	+30 43 22.77	11.″95	8.″28	5.68	3.93	90	1	69 ± 9
	NGC 4676A	12 46 09.850	+30 43 55.24	14.″04	11.″28	6.67	5.59	0	1	68 ± 9
Arp 244	NGC 4038/9	12 01 53.451	−18 52 26.50	88.″32	69.″12	10.32	8.08	50	13	50307 ± 248
Arp 256	NED01	0 18 51.025	−10 22 34.62	14.″33	12.″67	7.62	6.73	140	1	120 ± 11
Arp 259	NED 03/04	5 01 38.006	−4 15 29.55	27.″32	22.″31	7.29	5.95	90	1	262 ± 19
Arp 261	NED01	14 49 31.021	−10 10 32.23	46.″16	32.″49	6.49	4.57	250	1	110 ± 19
Arp 270	NGC 3395	10 49 50.028	+32 58 55.07	36.″54	27.″19	5.14	3.82	315	7	274 ± 22
	NGC 3396	10 49 55.286	+32 59 26.47	17.″91	6.″19	2.52	0.85	160	1	135 ± 12
Arp 283	NGC 2798	9 17 22.830	+41 59 59.55	17.″55	15.″13	2.55	2.20	345	1	65 ± 9
Arp 284	NGC 7714	23 36 14.310	+2 09 14.05	35.″65	16.″66	6.74	3.15	349	13	971 ± 33
Arp 293	NGC 6286	16 58 31.581	+58 56 15.77	28.″09	19.″71	11.17	7.84	231	7	260 ± 17
Arp 295	ARP 295B	23 42 00.805	−3 36 53.46	14.″22	11.″23	6.48	5.12	350	1	59 ± 8
Arp 299	NGC 3690	11 28 32.174	+58 33 46.26	68.″30	45.″99	15.90	10.71	330	13	7161 ± 90
IRAS 17208-0014	IRAS F17207-0014	17 23 21.953	−0 17 01.90	17.″49	9.″52	15.52	8.45	15	5	115 ± 13
IRAS 23128-5919	ESO 148-IG002	23 15 46.922	−59 03 14.16	16.″25	12.″74	14.50	11.37	260	13	220 ± 16
Mrk 231	UGC 08058	12 56 14.547	+56 52 24.67	20.″09	17.″68	17.35	15.27	105	13	3349 ± 63
Mrk 273	UGC 08696	13 44 42.002	+55 53 12.22	49.″60	24.″25	38.61	18.88	100	13	1121 ± 36
NGC 034	NGC 17	0 11 06.714	−12 06 27.79	20.″74	20.″02	7.98	7.70	120	1	61 ± 8
NGC 1700	MGC-01-13-038	04 56 56.452	−04 51 59.57	62.″77	44.″22	15.98	11.26	20	13	1714 ± 49
NGC 2207/IC 2163	NGC 2207/IC 2163	06 16 22.134	−21 22 21.18	66.″36	38.″06	12.23	7.01	15	13	786 ± 34
NGC 2865	ESO 498-G001	9 23 30.226	−23 09 44.13	21.″50	12.″20	3.95	2.24	240	1	75 ± 10
NGC 3256	NGC 3256N/S	10 27 51.096	−43 54 09.37	41.″22	39.″40	7.40	7.07	0	13	5702 ± 80
NGC 3353	UGC 05860	10 45 22.210	+55 57 35.61	38.″14	27.″79	3.42	2.49	357	1	50 ± 10
NGC 5018	UGCA 335	13 13 01.040	−19 31 04.39	23.″09	13.″44	4.30	2.50	5	7	283 ± 18
NGC 5256	NED01/02	13 38 18.085	+48 16 38.52	40.″00	32.″57	23.45	19.10	90	13	637 ± 27
NGC 6240	UGC 10592	16 52 58.527	+2 24 04.36	48.″65	33.″88	25.67	17.88	120	13	10518 ± 112
NGC 7592	NGC 7592A/B	23 18 22.276	−4 24 57.89	23.″67	22.″16	11.42	10.70	315	5	126 ± 12
UGC 5101	CGCG 289-001	9 35 51.539	+61 21 11.26	24.″01	14.″18	19.13	11.30	90	1	134 ± 13
UGC 5189	UGC 5189 NED01	9 42 53.329	+9 29 38.77	10.″48	10.″40	2.49	2.47	5	1	179 ± 15
	UGC 5189 NED02	9 42 56.660	+9 28 17.30	20.″39	4.″40	4.84	1.11	45	1	57 ± 10

Note.
[a] The position angle of the major axis defined south of east as in the *ds9* software.

overall X-ray luminosity of the galaxy. This could lead to a bias in the analysis, producing larger volumes of hot gas for longer observations, which will affect the derivation of the electron densities and therefore the masses of hot gas. Because this is an archival sample, there is a large galaxy-to-galaxy variation in the observing times used.

To circumvent this issue, it is desirable to use a consistent definition for the radius from galaxy to galaxy. In past studies

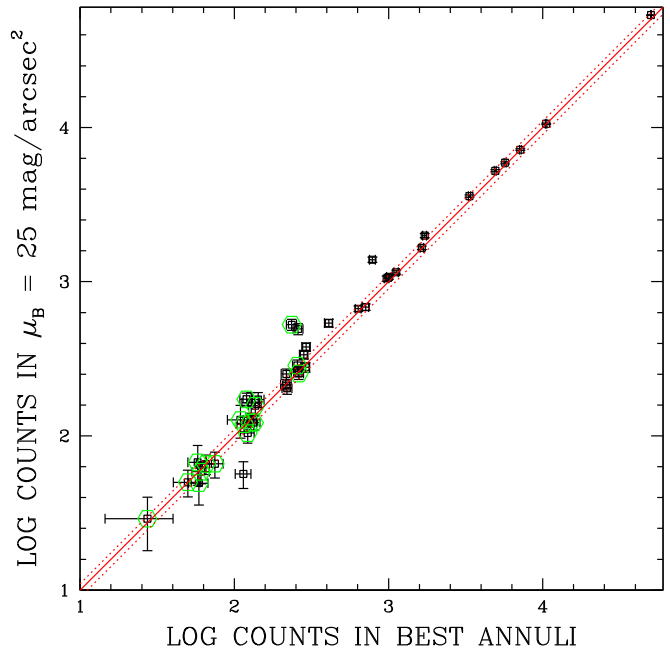

Figure 8. Comparison of soft (0.3–1 keV) X-ray counts within the $\mu_B = 25$ mag arcsec^{-2} isophote, and within our best determination of the angular extent of the X-ray emission. The solid line is the one-to-one relation, while the dotted lines represent ±10% variations. Galaxies marked with open green hexagons are systems with low S/N for which we used the single aperture method to get the sizes.

of the hot gas distribution of galaxies, a number of different methods have been used to determine the volume of hot gas. For example, Boroson et al. (2011) and Goulding et al. (2016) measured the extent out to which the diffuse emission equals the background. McQuinn et al. (2018) used a similar method, measuring the extent out to which the diffuse emission is detected at a 2σ level. Other groups measured the emission within the optical D25 isophote or the optical effective radius, and used this extent as the X-ray size in deriving electron densities (Mineo et al. 2012b; Su et al. 2015; Gaspari et al. 2019). A third method was used by Strickland et al. (2004a) and Grimes et al. (2005), who used the radius that encloses a given fraction of the total 0.3–1.0 keV flux. They found that the 90% enclosed-light fraction corresponds to an 0.3–1.0 keV surface brightness between approximately $\sim 10^{-9}$–10^{-8} photons s^{-1} cm^{-2} arcsec^{-2} for their sample galaxies.

Because our data set is so heterogeneous, after some experimentation, we chose to measure the radial extent out to a consistent 0.3–1.0 keV surface brightness level for all of the sample galaxies. To decide on this level, we explored how the enclosed-light fraction varies with different surface brightness cutoffs, assuming that the counts within the optical *B* band 25 mag arcsec^{-2} isophote constitute the "total" flux (this issue is discussed further below). Upon experimentation, we found that, for most galaxies, a 0.3–1.0 keV surface brightness cutoff of 3×10^{-9} photons s^{-1} cm^{-2} arcsec^{-2} produced counts that agreed with the total counts within 10%. This is consistent with the Grimes et al. (2005) and Strickland et al. (2004a) results for their 90% enclosed-light fractions.

There were 18 systems that were detected in the MEKAL component in Paper I but had too few counts for us to derive an acceptable radial profile. For these galaxies, we derived approximate sizes by starting with the initial elliptical regions chosen by eye, and then iteratively increasing the size of the ellipse by 30% until the galaxy was detected at the $\geqslant 2\sigma$ level and the 0.3–1.0 keV counts in the expanded ellipse equaled those in the $\mu_B = 25$ mag arcsec^{-2} isophote within the uncertainties. For the widely separated premerger pairs with two distinct regions of hot gas within the two optical galaxies, the two galaxies in the pair were treated separately in this procedure.

Four of the galaxies for which we could not find a radial profile (Arp 163, Arp 235, Arp 243, and Arp 263) were undetected in the MEKAL component in Paper I. These four galaxies are not included in any of the subsequent plots in this paper that involve quantities derived from the spatial size of the X-ray emission. Another galaxy, UGC 02238, was nominally detected in the MEKAL component at the 2.6σ level in the spectral decomposition in Paper I. However, it was not detected within the optical extent of the galaxy at the 2σ level in the 0.3–1.0 keV map. It is also omitted from the subsequent analysis in the current paper. Another system, UGC 05189, was undetected in the MEKAL component in Paper I. However, we detected the inner disks of both galaxies in the pair at the 5σ level in the 0.3–1.0 keV map. The area covered by the diffuse gas is considerably smaller than the optical extent, which might explain the nondetection in the spectral decomposition.

Except for the five systems for which we could not derive radial profiles, the *Chandra* 0.3–1.0 keV maps of the sample galaxies are displayed in the Appendix of this paper (Figures 20–27). In Table 3, we provide the central coordinates, major and minor axis radii, and position angles of the final ellipses derived using the methods described above, with the *dmextract*-derived sizes at 3×10^{-9} photons s^{-1} cm^{-2} arcsec^{-2} level. Table 3 also gives the number of annuli used in the radial profile (13, 7, 5, or 1). For systems with two distinct regions of diffuse emission, two ellipses are given in Table 3. In those cases, the name of the specific galaxy in the pair associated with the particular region is identified in the second column of Table 3. When the X-ray flux only comes from one galaxy in a pair, the name of that individual galaxy is listed in Table 3. If both galaxies in a pair are covered by a single region of diffuse emission, both names are given in the second column of Table 3. If there is only one galaxy in the system, the second column gives an alternative name for the galaxy. Table 3 also provides the point-source-subtracted, background-subtracted 0.3–1.0 keV counts in the final ellipse. Table 3 does not include UGC 02238 or the four systems without radial profiles that are undetected in the thermal component in Paper I. The final ellipses are superimposed on images of the galaxies in the Appendix of the paper.

In Figure 8, we compare the background-subtracted 0.3–1.0 keV counts obtained within the $\mu_B = 25$ mag arcsec^{-2} isophote with those extracted within the Table 3 radial extents. The solid line on this plot is the one-to-one relation, and the dashed lines mark ±10% differences. The systems marked by green hexagons in Figure 8 are those for which we were not able to find a radius using a set of concentric annuli. For most of the galaxies in the sample, the two measurements of the X-ray counts agree within the uncertainties with the range marked by the dotted lines. For only one system, IRAS 17208-0014, does our total count in the 3×10^{-9} photons s^{-1} arcsec^{-2} isophote exceed that in the optical isophotes by 10% or more, taking into account the uncertainties (i.e., only one system lies below the bottom dotted line). For IRAS 17208-0014, the X-ray radial extent in Table 3 exceeds the optical D25 size by a factor of 1.5, and the

Table 4
Outer (2σ) Ellipses for Galaxies with High-S/N Observations

Name	R.A. (J2000)	Decl. (J2000)	Major Axis Radius ($''$)	Minor Axis Radius ($''$)	Major Axis Radius (kpc)	Minor Axis Radius (kpc)	P.A.[a] (deg)	Diffuse 0.3−1.0 keV Counts	0.3–1.0 keV Surface Brightness ($\times 10^{-10}$ Photons s^{-1} cm^{-2} $arcsec^{-2}$)
AM 2055-425	20 58 26.554	−42 38 58.11	30.″20	13.″76	26.23	11.96	65	277 ± 19	⩽36.0
Arp 091	15 34 32.396	+15 11 36.55	15.″42	9.″90	2.54	1.63	300	233 ± 17	⩽116.0
Arp 148	11 03 53.839	+40 50 58.26	23.″24	13.″43	16.56	9.57	350	267 ± 18	⩽49.8
Arp 155	11 23 38.541	+53 50 30.51	41.″45	21.″08	9.25	4.70	350	167 ± 19	⩽19.9
Arp 157	1 24 34.398	+3 47 27.11	75.″10	24.″96	11.11	3.69	100	349 ± 27	⩽22.0
Arp 160	12 14 09.490	+54 31 32.96	49.″41	35.″13	9.35	6.64	258	1086 ± 36	⩽24.7
Arp 217	10 38 45.964	+53 30 08.73	99.″33	89.″22	8.67	7.79	230	5270 ± 80	⩽10.9
Arp 220	15 34 57.578	+23 30 06.07	54.″70	38.″34	22.02	15.44	15	851 ± 38	⩽16.6
Arp 222	23 39 53.876	−12 17 34.61	46.″63	27.″55	5.90	3.49	40	128 ± 16	⩽33.5
Arp 226	22 20 44.774	−24 40 41.77	12.″13	9.″67	3.94	3.14	30	217 ± 16	⩽106.6
Arp 236	01 07 46.897	−17 30 26.91	28.″52	28.″43	11.20	11.17	90	1652 ± 42	⩽18.1
Arp 244	12 01 53.451	−18 52 26.50	143.″52	112.″32	16.78	13.13	50	55121 ± 292	⩽2.4
Arp 270	10 49 50.028	+32 58 55.07	42.″63	31.″73	60	4.46	315	319 ± 24	⩽32.4
Arp 284	23 36 14.310	+2 09 14.05	57.″93	27.″07	10.96	5.12	349	1024 ± 36	⩽25.8
Arp 293	16 58 31.581	+58 56 15.77	32.″78	22.″99	13.03	9.14	231	262 ± 18	⩽59.6
Arp 299	11 28 32.174	+58 33 46.26	80.″72	54.″35	18.79	12.65	330	7434 ± 94	⩽13.0
IRAS 17208-0014	17 23 21.953	−0 17 01.90	23.″32	12.″69	20.69	11.27	15	101 ± 15	⩽29.4
IRAS 23128-5919	23 15 46.922	−59 03 14.16	11.″61	9.″10	10.36	8.12	260	214 ± 16	⩽55.7
Mrk 231	12 56 14.547	+56 52 24.67	65.″29	57.″46	56.40	49.64	105	5375 ± 109	⩽8.6
Mrk 273	13 44 42.002	+55 53 12.22	64.″48	31.″53	50.19	24.54	100	1212 ± 38	⩽18.8
NGC 1700	04 56 56.452	−04 51 59.57	102.″00	71.″86	25.97	18.30	20	2090 ± 62	⩽11.9
NGC 2207/ IC 2163	06 16 22.134	−21 22 21.18	119.″45	68.″50	22.01	12.63	15	1401 ± 52	⩽12.0
NGC 3256	10 27 51.096	−43 54 09.37	54.″95	52.″53	9.86	9.43	0	5918 ± 84	⩽16.6
NGC 5018	13 13 01.040	−19 31 04.39	23.″09	13.″44	4.30	2.50	5	283 ± 18	⩽53.9
NGC 5256	13 38 18.085	+48 16 38.52	51.″99	42.″34	30.49	24.82	90	672 ± 29	⩽29.9
NGC 6240	16 52 58.527	+2 24 04.36	90.″35	62.″91	47.67	33.20	120	12936 ± 141	⩽8.3
NGC 7592	23 18 22.276	−4 24 57.89	31.″56	29.″55	15.23	14.26	315	124 ± 13	⩽37.1

Note.
[a] The position angle of the major axis defined south of east as in the *ds9* software.

0.3–1.0 keV counts within the Table 3 ellipse are about 2.2 times those within the optical isophotes.

Taking into account the uncertainties, four systems in our sample have counts within the "best" radii that are 60–80% of the counts within the optical extent, and one (UGC 05189) has counts within the "best" radii that are 50% of the counts in the optical isophotes. These systems lie above the top dotted line in Figure 8. Most of these systems are galaxy pairs that have two distinct regions of X-ray emission within the $\mu_B = 25$ mag $arcsec^{-2}$ isophote. Very faint diffuse emission outside of these regions may contribute to the total counts in the optical extent. This faint emission likely does not contribute much to the overall mass of hot gas in the system.

For all but one of our systems, we can measure X-ray emission beyond the 3×10^{-9} photons s^{-1} cm^{-2} $arcsec^{-2}$ isophote in our *dmextract* radial profiles. For completeness, we provide the full (2σ) extent of the X-ray emission for these systems in Table 4. In all but 11 of these cases, the 2σ extent of the diffuse X-ray emission is at least 20% larger than the optical D25 size. The most extreme case is Mrk 231, for which the ratio of the 2σ X-ray radius divided by the maximum $\mu_B = 25$ mag $arcsec^{-2}$ radius is 2.6. For Mrk 231, the counts within the 2σ extent are about 1.5 times those in the D25 radius. Although the measured 2σ X-ray sizes are often larger than the D25 extent, the 0.3–1.0 keV counts within the 2σ radius are generally less than or consistent with the counts within the D25 radius. This means that the emission outside of D25 does not contribute significantly to the total flux.

5. Volume and Mass of Hot Gas, Electron Densities, and Filling Factor

We calculated the volume of hot gas for each system in the sample, assuming that the hot gas distribution has an ellipsoidal structure with the third dimension equal to the average of the other two. For these calculations, we use the X-ray sizes at the 3×10^{-9} photons s^{-1} $arcsec^{-2}$ isophote as discussed above (Table 3). For the premerger systems for which we could measure two distinct regions of hot gas, we calculated the sum of the two volumes.

The uncertainty in the geometry of the hot gas likely contributes scatter to the relationships shown below. Although the true three-dimensional distribution of the hot gas in a particular galaxy is unknown, we can use the statistics of the observed ellipticities of the diffuse X-ray emission on the sky (Table 3) to make a rough estimate of the average uncertainty in the volume, assuming random orientations in space. The average major/minor axial ratio of the diffuse X-ray emission on the sky is 1.50, with a root mean square (rms) of 0.39. We therefore assume that the line-of-sight dimension, on average, will range from 1.5 times greater to 1.5 times smaller than the

average of the other two dimensions. Thus, we assume that our estimates of the volume are uncertain by a factor of 1.5.

Using the derived volumes of hot gas, we estimated electron densities in the hot gas as a function of filling factor. For this calculation, we used the relation $L_X(\mathrm{gas}) = \Lambda n_e\ ^2 fV$, where L_X(gas) is the absorption-corrected 0.3–8.0 keV X-ray luminosity of the hot gas from Paper I (the MEKAL component), Λ is the cooling function (McKee & Cowie 1977; McCray 1987), V is the volume of gas, n_e is the electron density, and f is the filling factor. In this calculation, we assumed that the number of hydrogen atoms $\sim n_e$. The derived gas masses depend upon the temperature of the X-ray-emitting gas. Unfortunately, we were able to obtain a fit for the gas temperature for only 15 systems in Paper I (see Table 5 in that paper). For the remaining systems, we assumed a temperature of 0.3 keV. In Section 6.5 of this paper, we investigate how this assumption affects our results. In calculating n_e, we neglect X-ray emission outside of the 0.3–8.0 keV *Chandra* bandpass. However, emission outside of this range may also contribute to cooling the gas. In Section 6.5, we discuss this approximation and how it depends upon temperature.

From the X-ray luminosity, the volume, and the temperature, we derive $n_e\sqrt{f}$ for our sample galaxies; we are not able to independently determine n_e and f. We find that $n_e\sqrt{f}$ ranges from 1.1×10^{-3}–$2.2 \times 10^{-2}\,\mathrm{cm}^{-3}$, similar to the values found by Mineo et al. (2012b) for their spirals. Accounting for the uncertainty in volume and conservatively assuming a factor of two uncertainty in L_X(gas) (due in part to uncertainties in separating the thermal and nonthermal emission; see Section 5.3 in Paper I), propagation of errors implies that our estimates of $n_e\sqrt{f}$ are uncertain by a factor of 1.8 on average.

The radiative cooling times for the hot gas (i.e., total thermal energy divided by L_X(gas)) in these galaxies range from 16 to 700 Myr, with a median time of about 60 Myr. These are similar to the Mineo et al. (2012b) estimates for disk galaxies. We then calculated the mass of the hot X-ray-emitting gas $M_X(\mathrm{gas}) = m_p n_e V$, where m_p is the mass of a proton. Accounting for the uncertainties in V and n_e, we adopt an uncertainty in our estimates of M_X(gas) of a factor of two, not including the uncertainty in the filling factor.

6. Correlation Analysis

From the *Chandra* data, we derived a set of parameters for our sample galaxies, including the volume of hot gas, $n_e\sqrt{f}$, L_X(gas), and M_X(gas). From data at other wavelengths, we have another set of values for our galaxies, including SFR, SFE, L_{FIR}, L_K, L_{FIR}/L_K, [3.6]–[24], F_{60}/F_{100}, $M_{H\,I}/M_{H_2}$, and the merger stage. Combining these two sets, we derive additional parameters, including L_X(gas)/SFR, M_X(gas)/SFR, and $M_X(\mathrm{gas})/(M_{H_2}+M_{H\,I})$. In this section, we correlate these parameters against each other, and calculate the best-fit linear log versus log relations for various combinations of these parameters. In Paper I, we found that some trends change at low SFRs, so we did these fits for two cases: the full range of SFRs and the subset of systems with SFR $> 1\,M_\odot\,\mathrm{yr}^{-1}$.

For each relation, we calculated the rms deviation from the best-fit line and the Spearman rank order coefficient. These values are compiled in Table 5, along with the best-fit parameters. For comparison with the Spearman coefficients, Table 5 also provides Pearson correlation coefficients, assuming a linear relationship between the two parameters. The two types of correlation coefficients agree fairly well for our sample

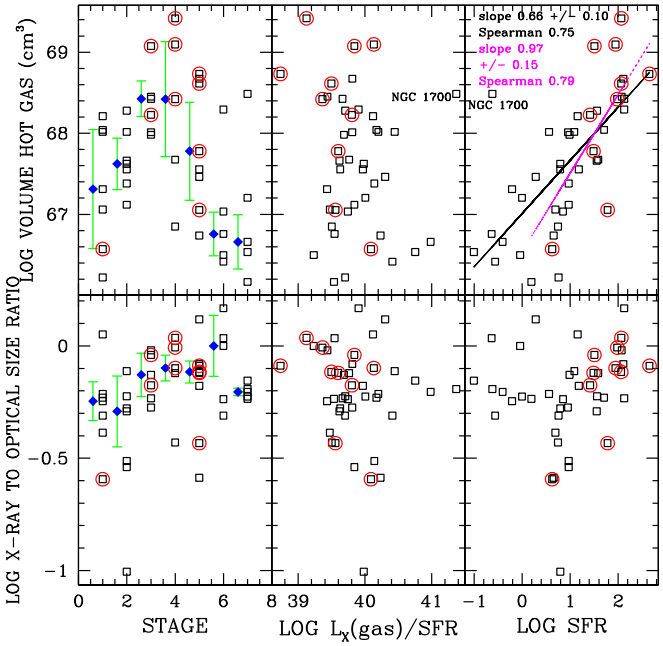

Figure 9. Plots of X-ray volume (top row) and X-ray/optical size ratio (bottom row) vs. merger stage (first column), L_X/SFR (second column), and SFR (third column). The best-fit line is plotted in the top right panel. Black open squares mark the sample galaxies, with those circled by red circles being AGN. In the left column of plots, the filled blue diamonds are the median values for each stage, slightly offset to the left. The error bars plotted on the median values display the semi-interquartile range, equal to half the difference between the 75th percentile and the 25th percentile.

(see Table 5). In Table 5, we classified the relations, into "strong correlation," "weak correlation," or "no correlation." We defined a "strong correlation" as one in which the Spearman coefficient is greater than 0.55 (i.e., $\leqslant$0.1% likelihood of happening by chance), and a "strong anticorrelation" is one in which the Spearman coefficient is less than −0.55. A "weak correlation" is one in which the Spearman coefficient is between 0.35 and 0.55, where 0.35 corresponds to a ∼5% probability of happening by chance. A "weak anticorrelation" implies a Spearman coefficient between −0.35 and −0.55, and "no correlation" means a Spearman coefficient between −0.35 and 0.35.

The most important of the correlations are plotted in Figures 9–19. For convenience, when a plot is shown, the number of the figure that displays each correlation is provided in Table 5, along with the best-fit parameters and the Spearman/Pearson coefficients. For clarity of presentation, we do not include error bars on the plots. As discussed above, we estimate that our values of M_X(gas) are uncertain by about a factor of two. This means that the uncertainty in $\log(M_X(\mathrm{gas}))$ is about 0.3 dex. The rms uncertainties on some of the fits involving $\log(M_X(\mathrm{gas}))$ are close to or slightly larger than this estimate (see Table 5), so the uncertainty in M_X(gas) may be a limiting factor in this analysis. Because the uncertainty in the CO/H_2 ratio is potentially an even larger factor, we do the correlations for both CO/H_2 ratios. This provides a test of whether the results are biased by the choice of CO/H_2 ratios.

As another test, we also ran the correlation analysis using radii and volumes determined from the *specextract/ISIS* radial profiles rather than *dmextract*. The best-fit relations and correlation coefficients changed slightly, but the basic

Table 5
Correlations and Anticorrelations

Fig Num	SFR Range	CO/H_2 Ratio	Relation	rms	Spear/ Pearson Coeff.	Correl.
			Basic Relations			
2	all		LOG SFR = (0.79 ± 0.21) LOG L_K − (7.75 ± 2.29)	0.76	0.47/0.51	weak
2	>1 $M_\odot$ yr^{-1}		LOG SFR = (0.84 ± 0.19) LOG L_K − (8.05 ± 2.09)	0.48	0.51/0.62	weak
2	all		LOG SFR = (0.88 ± 0.11) LOG (L_{FIR}/L_K) + (1.33 ± 0.1)	0.56	0.79/0.77	strong
2	>1 $M_\odot$ yr^{-1}		LOG SFR = (0.95 ± 0.16) LOG (L_{FIR}/L_K) + (1.46 ± 0.08)	0.42	0.75/0.72	strong
2	all		LOG SFR = (0.41 ± 0.05) ([3.6]–[24]) − (1.74 ± 0.33)	0.53	0.81/0.80	strong
2	>1 $M_\odot$ yr^{-1}		LOG SFR = (0.41 ± 0.07) ([3.6]–[24]) − (1.62 ± 0.5)	0.43	0.76/0.72	strong
2	all		LOG SFR = (3.46 ± 0.76) LOG (F_{60}/F_{100}) + (1.49 ± 0.15)	0.70	0.60/0.58	strong
2	>1 $M_\odot$ yr^{-1}		LOG SFR = (2.17 ± 0.69) LOG (F_{60}/F_{100}) + (1.55 ± 0.12)	0.54	0.50/0.48	weak
4	all	Const	LOG SFE = (2.54 ± 0.47) LOG (F_{60}/F_{100}) − (8.12 ± 0.09)	0.42	0.72/0.67	strong
4	>1 $M_\odot$ yr^{-1}	Const	LOG SFE = (2.93 ± 0.48) LOG (F_{60}/F_{100}) − (8.13 ± 0.08)	0.37	0.76/0.74	strong
4	all	Var	LOG SFE = (3.38 ± 0.55) LOG (F_{60}/F_{100}) − (7.68 ± 0.11)	0.49	0.73/0.72	strong
4	>1 $M_\odot$ yr^{-1}	Var	LOG SFE = (3.60 ± 0.63) LOG (F_{60}/F_{100}) − (7.66 ± 0.11)	0.49	0.71/0.71	strong
4	all	Const	LOG SFE = (0.23 ± 0.11) LOG SFR − (8.72 ± 0.16)	0.53	0.40/0.33	weak
4	>1 $M_\odot$ yr^{-1}	Const	LOG SFE = (0.37 ± 0.14) LOG SFR − (8.95 ± 0.21)	0.50	0.44/0.42	weak
4	all	Var	LOG SFE = (0.61 ± 0.10) LOG SFR − (8.82 ± 0.15)	0.50	0.75/0.71	strong
4	>1 $M_\odot$ yr^{-1}	Var	LOG SFE = (0.88 ± 0.13) LOG SFR − (9.24 ± 0.19)	0.43	0.77/0.78	strong
			Comparisons with Volume			
9	all		LOG VOLUME = (0.66 ± 0.10) LOG SFR + (67.01 ± 0.14)	0.59	0.75/0.70	strong
9	>1 $M_\odot$ yr^{-1}		LOG VOLUME = (0.97 ± 0.15) LOG SFR + (66.54 ± 0.22)	0.52	0.79/0.75	strong
10	all	Const	LOG VOLUME versus LOG SFE	0.85	0.16/0.06	none
10	all	Var	LOG VOLUME = (0.57 ± 0.18) LOG SFE + (72.36 ± 1.48)	0.75	0.53/0.47	weak
10	all		LOG VOLUME versus LOG (F_{60}/F_{100})	0.79	0.34/0.29	none
10	>1 $M_\odot$ yr^{-1}		LOG VOLUME versus LOG (F_{60}/F_{100})	0.78	0.20/0.11	none
11	all		LOG VOLUME = (0.80 ± 0.12) LOG L_X(gas) + (35.11 ± 4.85)	0.57	0.79/0.72	strong
11	all		LOG VOLUME = (−1.19 ± 0.39) LOG ($n_e\sqrt{f}$) + (64.95 ± 0.9)	0.75	−0.39/−0.43	weak anti
11	all		LOG VOLUME = (0.85 ± 0.18) LOG L_K + (58.23 ± 2.01)	0.67	0.65/0.59	strong
11	>1 $M_\odot$ yr^{-1}		LOG VOLUME = (1.15 ± 0.23) LOG L_K + (54.92 ± 2.58)	0.60	0.65/0.66	strong
11	all		LOG VOLUME = (0.40 ± 0.15) LOG (L_{FIR}/L_K) + (67.81 ± 0.13)	0.77	0.49/0.37	weak
none	all		LOG VOLUME = (0.17 ± 0.07) ([3.6]–[24]) + (66.5 ± 0.48)	0.77	0.44/0.36	weak
none	all		LOG (VOLUME/SFR) versus LOG SFR	0.59	−0.34/−0.46	none
none	>1 $M_\odot$ yr^{-1}		LOG (VOLUME/SFR) versus LOG SFR	0.52	0.02/−0.04	none
none	all		LOG (VOLUME/L_K) = (0.32 ± 0.11) LOG SFR + (56.27 ± 0.14)	0.61	0.40/0.42	weak
none	>1 $M_\odot$ yr^{-1}		LOG (VOLUME/L_K) = (0.52 ± 0.15) LOG SFR + (55.97 ± 0.21)	0.51	0.51/0.53	weak
none	all		LOG (VOLUME/L_K) versus LOG L_K	0.67	0.02/−0.13	none
none	>1 $M_\odot$ yr^{-1}		LOG (VOLUME/L_K) versus LOG L_K	0.60	0.16/0.12	none
			Comparisons with LOG (L_X(gas)/SFR)			
none	all		LOG (L_X(gas)/SFR) versus LOG SFR	0.40	−0.35/−0.53	none
none	>1 $M_\odot$ yr^{-1}		LOG (L_X(gas)/SFR) versus LOG SFR	0.30	−0.35/−0.48	none
none	all		LOG (L_X(gas)/SFR) = (−1.69 ± 0.37) LOG (F_{60}/F_{100}) + (39.6 ± 0.07)	0.34	−0.53/−0.58	weak anti
none	>1 $M_\odot$ yr^{-1}		LOG (L_X(gas)/SFR) = (−1.28 ± 0.38) LOG (F_{60}/F_{100}) + (39.64 ± 0.07)	0.30	−0.45/−0.50	weak anti
none	all	Const	LOG (L_X(gas)/SFR) = (−0.40 ± 0.10) LOG SFE + (36.39 ± 0.81)	0.32	−0.55/−0.58	weak anti
none	>1 $M_\odot$ yr^{-1}	Const	LOG (L_X(gas)/SFR) = (−0.36 ± 0.09) LOG SFE + (36.76 ± 0.8)	0.29	−0.49/−0.56	weak anti
none	all	Var	LOG (L_X(gas)/SFR) = (−0.32 ± 0.08) LOG SFE + (37.22 ± 0.63)	0.32	−0.55/−0.57	weak anti
none	>1 $M_\odot$ yr^{-1}	Var	LOG (L_X(gas)/SFR) = (−0.27 ± 0.07) LOG SFE + (37.58 ± 0.61)	0.29	−0.52/−0.55	weak anti
			Comparisons with LOG M_X(gas) and LOG M_X(gas)/SFR			
13	all		LOG M_X(gas) = (0.70 ± 0.07) LOG SFR + (7.6 ± 0.1)	0.42	0.86/0.83	strong
13	>1 $M_\odot$ yr^{-1}		LOG M_X(gas) = (0.88 ± 0.10) LOG SFR + (7.35 ± 0.14)	0.34	0.86/0.84	strong
13	all		LOG M_X(gas) = (0.94 ± 0.14) LOG L_K − (2.05 ± 1.58)	0.53	0.69/0.72	strong
13	>1 $M_\odot$ yr^{-1}		LOG M_X(gas) = (1.00 ± 0.17) LOG L_K − (2.68 ± 1.94)	0.45	0.67/0.71	strong
13	all		LOG (M_X(gas)/SFR) = (−0.30 ± 0.07) LOG SFR + (7.6 ± 0.1)	0.42	−0.38/−0.53	weak anti
13	>1 $M_\odot$ yr^{-1}		LOG (M_X(gas)/SFR) versus LOG SFR	0.34	−0.12/−0.22	none
13	all		LOG (M_X(gas)/SFR) versus LOG L_K	0.49	0.28/0.17	none
13	>1 $M_\odot$ yr^{-1}		LOG (M_X(gas)/SFR) = (0.16 ± 0.13) LOG L_K + (5.37 ± 1.48)	0.34	0.37/0.21	weak

Table 5
(Continued)

Fig Num	SFR Range	CO/H_2 Ratio	Relation	rms	Spear/ Pearson Coeff.	Correl.
14	all	Const	LOG (M_X(gas)/SFR) = (-0.37 ± 0.10) LOG SFE + (4.06 ± 0.84)	0.33	$-0.52/-0.54$	weak anti
14	$>1\ M_\odot\ yr^{-1}$	Const	LOG (M_X(gas)/SFR) = (-0.33 ± 0.10) LOG SFE + (4.38 ± 0.85)	0.31	$-0.45/-0.51$	weak anti
14	all	Var	LOG (M_X(gas)/SFR) = (-0.26 ± 0.08) LOG SFE + (5.11 ± 0.68)	0.35	$-0.42/-0.46$	weak anti
14	$>1\ M_\odot\ yr^{-1}$	Var	LOG (M_X(gas)/SFR) versus LOG SFE	0.33	$-0.34/-0.39$	none
14	all		LOG (M_X(gas)/SFR) = (-0.22 ± 0.03) ([3.6]–[24]) + (8.78 ± 0.19)	0.31	$-0.66/-0.77$	strong anti
14	$>1\ M_\odot\ yr^{-1}$		LOG (M_X(gas)/SFR) = (-0.17 ± 0.05) ([3.6]–[24]) + (8.41 ± 0.35)	0.30	$-0.50/-0.52$	weak anti
14	all		LOG (M_X(gas)/SFR) = (-0.45 ± 0.07) LOG (L_{FIR}/L_K) + (7.13 ± 0.06)	0.35	$-0.51/-0.71$	weak anti
14	$>1\ M_\odot\ yr^{-1}$		LOG (M_X(gas)/SFR) versus LOG (L_{FIR}/L_K)	0.33	$-0.28/-0.33$	none
14	all		LOG (M_X(gas)/SFR) = (-1.66 ± 0.34) LOG(F_{60}/F_{100}) + (7.04 ± 0.07)	0.31	$-0.59/-0.61$	strong anti
14	$>1\ M_\odot\ yr^{-1}$		LOG (M_X(gas)/SFR) = (-1.33 ± 0.38) LOG (F_{60}/F_{100}) + (7.04 ± 0.07)	0.30	$-0.48/-0.51$	weak anti
14	all		LOG (M_X(gas)/SFR) versus LOG ($n_e\sqrt{f}$)	0.46	$-0.34/-0.38$	none
14	$>1\ M_\odot\ yr^{-1}$		LOG (M_X(gas)/SFR) = (-0.55 ± 0.20) LOG ($n_e\sqrt{f}$) + (5.97 ± 0.46)	0.32	$-0.39/-0.42$	weak anti
none	all		LOG (M_X(gas)/L_K) = (0.53 ± 0.07) LOG (SFR/L_K) + (2.54 ± 0.68)	0.33	0.77/0.77	strong
none	$>1\ M_\odot\ yr^{-1}$		LOG (M_X(gas)/L_K) = (0.67 ± 0.11) LOG (SFR/L_K) + (3.91 ± 1.09)	0.31	0.73/0.73	strong
none	all		LOG (M_X(gas)/L_K) = (0.37 ± 0.07) LOG SFR − (3.13 ± 0.1)	0.41	0.63/0.73	strong
none	$>1\ M_\odot\ yr^{-1}$		LOG (M_X(gas)/L_K) = (0.42 ± 0.10) LOG SFR − (3.22 ± 0.15)	0.37	0.62/0.73	strong
none	all		LOG (M_X(gas)/L_K) versus LOG L_K	0.52	0.01/−0.07	none
none	$>1\ M_\odot\ yr^{-1}$		LOG (M_X(gas)/L_K) versus LOG L_K	0.45	0.04/0.00	none
none	all		LOG (M_X(gas)/SFR) = (0.47 ± 0.07) LOG (L_K/SFR) + (2.54 ± 0.68)	0.33	0.58/0.74	strong
none	$>1\ M_\odot\ yr^{-1}$		LOG (M_X(gas)/SFR) = (0.33 ± 0.11) LOG (L_K/SFR) + (3.91 ± 1.09)	0.31	0.41/0.46	weak
none	all	Const	LOG (M_X(gas)/SFR) versus LOG ($M_{H\,I}/M_{H_2}$)	0.48	−0.30/−0.27	none
none	all	Var	LOG (M_X(gas)/SFR) versus LOG ($M_{H\,I}/M_{H_2}$)	0.48	−0.31/−0.27	none
none	all		LOG (M_X(gas)/SFR) versus LOG VOLUME	0.49	0.17/0.16	none
			Comparisons with LOG (M_X(gas)/(M_{H_2}+$M_{H\,I}$))			
15	all	Const	LOG (M_X(gas)/(M_{H_2}+$M_{H\,I}$)) = (0.25 ± 0.10) LOG SFR − (2.05 ± 0.13)	0.41	0.50/0.42	weak
15	$>1\ M_\odot\ yr^{-1}$	Const	LOG (M_X(gas)/(M_{H_2}+$M_{H\,I}$)) = (0.58 ± 0.14) LOG SFR − (2.49 ± 0.19)	0.37	0.71/0.65	strong
15	all	Var	LOG (M_X(gas)/(M_{H_2}+$M_{H\,I}$)) = (0.40 ± 0.12) LOG SFR − (2.07 ± 0.15)	0.48	0.65/0.54	strong
15	$>1\ M_\odot\ yr^{-1}$	Var	LOG (M_X(gas)/(M_{H_2}+$M_{H\,I}$)) = (0.82 ± 0.16) LOG SFR − (2.64 ± 0.21)	0.41	0.80/0.73	strong
15	all	Const	LOG (M_X(gas)/(M_{H_2}+$M_{H\,I}$)) versus LOG SFE	0.43	0.35/0.32	none
15	$>1\ M_\odot\ yr^{-1}$	Const	LOG (M_X(gas)/(M_{H_2}+$M_{H\,I}$)) = (0.35 ± 0.17) LOG SFE + (1.21 ± 1.45)	0.45	0.48/0.40	weak
15	all	Var	LOG (M_X(gas)/(M_{H_2}+$M_{H\,I}$)) = (0.52 ± 0.13) LOG SFE + (2.6 ± 1.07)	0.45	0.61/0.61	strong
15	$>1\ M_\odot\ yr^{-1}$	Var	LOG (M_X(gas)/(M_{H_2}+$M_{H\,I}$)) = (0.60 ± 0.14) LOG SFE + (3.21 ± 1.16)	0.45	0.70/0.66	strong
16	all	Const	LOG (M_X(gas)/(M_{H_2}+$M_{H\,I}$)) versus LOG L_K	0.43	0.31/0.33	none
16	$>1\ M_\odot\ yr^{-1}$	Const	LOG (M_X(gas)/(M_{H_2}+$M_{H\,I}$)) versus LOG L_K	0.46	0.31/0.33	none
16	all	Var	LOG (M_X(gas)/(M_{H_2}+$M_{H\,I}$)) = (0.49 ± 0.22) LOG L_K − (7.12 ± 2.43)	0.52	0.41/0.40	weak
16	$>1\ M_\odot\ yr^{-1}$	Var	LOG (M_X(gas)/(M_{H_2}+$M_{H\,I}$)) = (0.60 ± 0.29) LOG L_K − (8.29 ± 3.23)	0.56	0.40/0.39	weak
16	all	Const	LOG (M_X(gas)/(M_{H_2}+$M_{H\,I}$)) versus LOG (F_{60}/F_{100})	0.44	0.29/0.24	none
16	$>1\ M_\odot\ yr^{-1}$	Const	LOG (M_X(gas)/(M_{H_2}+$M_{H\,I}$)) = (1.02 ± 0.66) LOG (F_{60}/F_{100}) − (1.68 ± 0.12)	0.46	0.44/0.31	weak
16	all	Var	LOG (M_X(gas)/(M_{H_2}+$M_{H\,I}$)) versus LOG (F_{60}/F_{100})	0.54	0.34/0.28	none
16	$>1\ M_\odot\ yr^{-1}$	Var	LOG (M_X(gas)/(M_{H_2}+$M_{H\,I}$)) = (1.32 ± 0.82) LOG (F_{60}/F_{100}) − (1.5 ± 0.15)	0.57	0.41/0.32	weak
17	all	Const	LOG (M_X(gas)/(M_{H_2}+$M_{H\,I}$)) versus ([3.6]–[24])	0.44	0.35/0.23	none
17	$>1\ M_\odot\ yr^{-1}$	Const	LOG (M_X(gas)/(M_{H_2}+$M_{H\,I}$)) = (0.20 ± 0.08) ([3.6]–[24]) − (3.21 ± 0.61)	0.44	0.54/0.44	weak
17	all	Var	LOG (M_X(gas)/(M_{H_2}+$M_{H\,I}$)) = (0.11 ± 0.07) ([3.6]–[24]) − (2.44 ± 0.46)	0.54	0.44/0.31	weak
17	$>1\ M_\odot\ yr^{-1}$	Var	LOG (M_X(gas)/(M_{H_2}+$M_{H\,I}$)) = (0.26 ± 0.10) ([3.6]–[24]) − (3.55 ± 0.74)	0.53	0.55/0.47	weak
17	all	Const	LOG (M_X(gas)/(M_{H_2}+$M_{H\,I}$)) = (0.19 ± 0.13) LOG (L_{FIR}/L_K) − (1.73 ± 0.1)	0.44	0.43/0.27	weak
17	$>1\ M_\odot\ yr^{-1}$	Const	LOG (M_X(gas)/(M_{H_2}+$M_{H\,I}$)) = (0.53 ± 0.20) LOG (L_{FIR}/L_K) − (1.68 ± 0.1)	0.42	0.61/0.49	strong
17	all	Var	LOG (M_X(gas)/(M_{H_2}+$M_{H\,I}$)) = (0.33 ± 0.16) LOG (L_{FIR}/L_K) − (1.56 ± 0.12)	0.53	0.54/0.36	weak
17	$>1\ M_\odot\ yr^{-1}$	Var	LOG (M_X(gas)/(M_{H_2}+$M_{H\,I}$)) = (0.74 ± 0.24) LOG (L_{FIR}/L_K) − (1.49 ± 0.12)	0.51	0.65/0.54	strong

conclusions of the paper were unchanged. The relations given below were derived from the *dmextract* results.

To see if our results are affected by the inclusion of Seyfert galaxies in the sample, we also calculated the correlations excluding the AGN. The correlation coefficients tend to be somewhat smaller with the smaller sample, but the basic results do not change and the important correlations discussed below still hold.

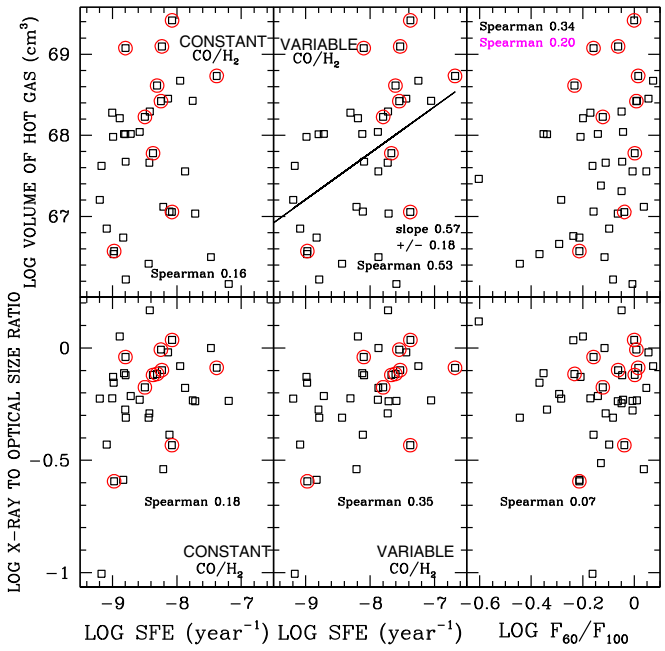

Figure 10. Plots of X-ray volume (top row) and X-ray/optical size ratio (bottom row) vs. SFE calculated with constant CO/H_2 ratio (first column), SFE calculated with variable CO/H_2 ratio (second column), and F_{60}/F_{100} ratio (third column). AGN are identified by red circles.

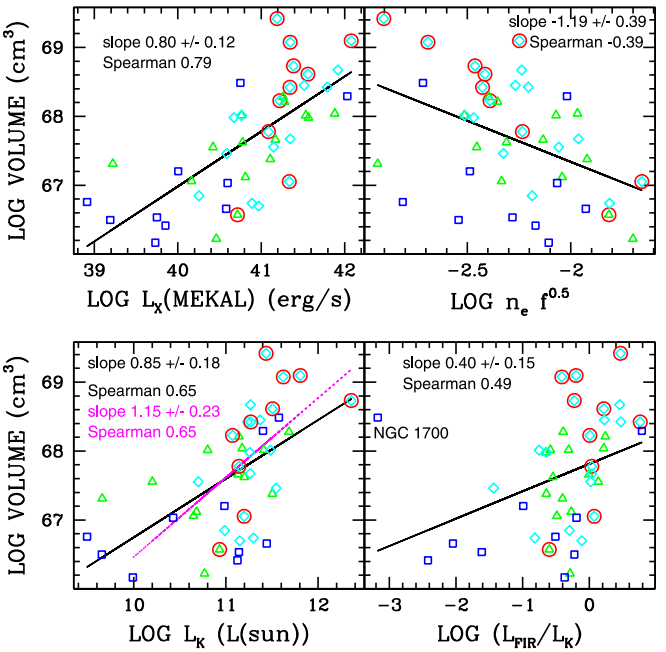

Figure 11. Top left: the volume of the hot gas plotted against L_X(gas). The best-fit line is plotted. Top right: the volume vs. $n_e\sqrt{f}$, where n_e is the electron density and f is the filling factor. Bottom left: volume vs. L_K. Bottom right: volume vs. L_{FIR}/L_K. Systems at merger stages 1 and 2 are marked as open green triangles. Merger stages 3, 4, and 5 are indicated by open cyan diamonds. Merger stages 6 and 7 are identified by blue open squares. AGN are identified by red circles.

6.1. Relations with Volume and with n_e

In the top row of Figure 9, we plot the volume of hot gas as a function of merger stage, L_X(gas)/SFR, and SFR. The bottom row of panels in this figure displays the ratio of the maximum radial extent of the X-ray emission to the maximum optical size as measured by the B band 25 mag arcsec^{-2} isophote against merger stage, L_X(gas)/SFR, and SFR. The first column of Figure 9 shows that stage 3 and stage 4 mergers tend to have large X-ray sizes and large X-ray/optical size ratios. This is a consequence of the bias toward higher SFRs in the midmerger stages. The second column shows little correlation between the volume of hot gas and L_X(gas)/SFR, or between the X-ray to optical size and L_X(gas)/SFR. Systems in which the X-ray extent exceeds that in the optical tend to have high SFRs (Figure 9, bottom right panel), but with a lot of scatter.

In Figure 9, the strongest correlation is seen in the top right panel: larger volumes of hot X-ray-emitting gas are found in higher-SFR systems. For the full set of galaxies, the best-fit slope is less than one. However, once low-SFR systems are excluded, the slope is consistent with one. Thus, low-SFR systems tend to have larger volumes than expected based on their SFRs.

We have marked the location of the late-stage merger NGC 1700 on the two upper right panels in Figure 9. It stands out in the sample for having a large volume of hot gas, compared to its SFR. This galaxy has a high L_K and a low SFR, with an elliptical appearance and tidal debris. It may be a system for which virialized hot gas in the gravitational potential contributes significantly to the observed diffuse X-ray-emitting gas. This system is discussed further in Section 7.4.

In Figure 10, we plot the volume of hot gas (top row) and the X-ray/optical size ratio (bottom row) against the SFE (first and second columns) and the F_{60}/F_{100} ratio (last column). The first column utilizes a constant CO/H_2 ratio, while the second uses the variable CO/H_2 ratio. This figure shows that the systems with large volumes tend to have large SFEs (when a variable CO/H_2 ratio is used). However, this is a very weak correlation with a lot of scatter; some systems with large SFEs have only moderate volumes and size ratios.

No significant correlation is seen between volume and F_{60}/F_{100} (Figure 10, upper right), despite the fact that volume is correlated with SFR (Figure 9), and F_{60}/F_{100} is correlated with SFR (Figure 2). However, the correlation between F_{60}/F_{100} and SFR is weak, with considerable scatter. The sample galaxies only cover a small range in log F_{60}/F_{100} (0.3 dex) while the SFR varies over two orders of magnitude. This means that uncertainties in the *IRAS* fluxes can make it difficult to detect a correlation. Instead of being directly dependent on SFR itself, theoretical models (e.g., Desert et al. 1990) suggest that the F_{60}/F_{100} ratio depends on the intensity of the ISRF. The average ISRF in a galaxy can vary greatly for a given global SFR of the galaxy, depending upon the spatial density of young stars. In contrast, the volume of hot gas in these galaxies depends directly upon the total number of young stars rather than on the spatial density of those stars.

The upper left panel of Figure 11 shows that the volume of hot gas is well-correlated with L_X(gas). The slope in this log–log plot is close to one. In the right panel of Figure 11, the volume is plotted against the derived $n_e\sqrt{f}$. There is a weak trend of decreasing $n_e\sqrt{f}$ with increasing volume.

In the lower left panel of Figure 11, we show that the volume is also correlated with L_K. However, the correlation is weaker than for volume versus SFR, and the scatter is larger (Table 5). This supports the idea that the volume of hot gas in this sample of galaxies is largely determined by the number of young stars, with the correlation of volume with L_K being a byproduct of the SFR–L_K correlation.

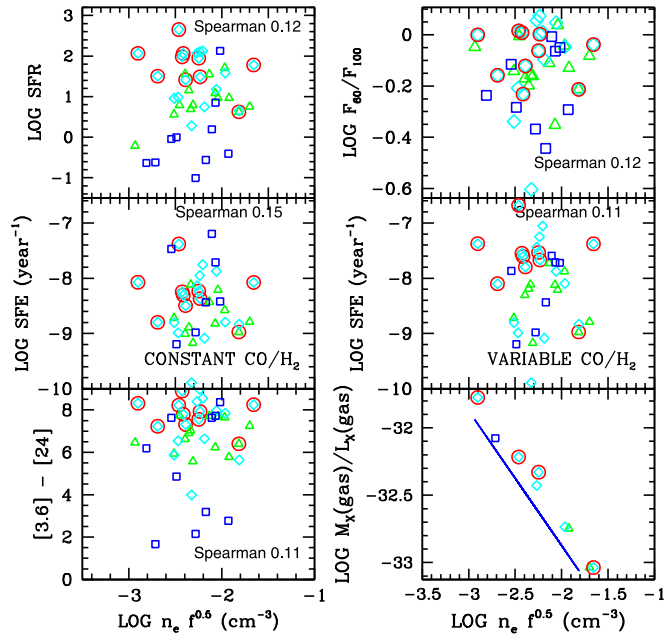

Figure 12. Upper left: SFR plotted against $n_e\sqrt{f}$. Upper right: F_{60}/F_{100} vs. $n_e\sqrt{f}$. The middle row compares SFE calculated with the two methods with $n_e\sqrt{f}$. Bottom left: [3.6]–[24] vs. $n_e\sqrt{f}$. Bottom right: $M_X(\mathrm{gas})/L_X(\mathrm{gas})$ vs. $n_e\sqrt{f}$ for the 15 systems with measured temperatures. The solid blue line in the lower right plot is the assumed relation, assuming a constant temperature of 0.3 keV. In these plots, n_e is the electron density and f is the filling factor. Systems at merger stages 1 and 2 are marked as open green triangles. Merger stages 3, 4, and 5 are indicated by open cyan diamonds. Merger stages 6 and 7 are identified by blue open squares. AGN are identified by red circles.

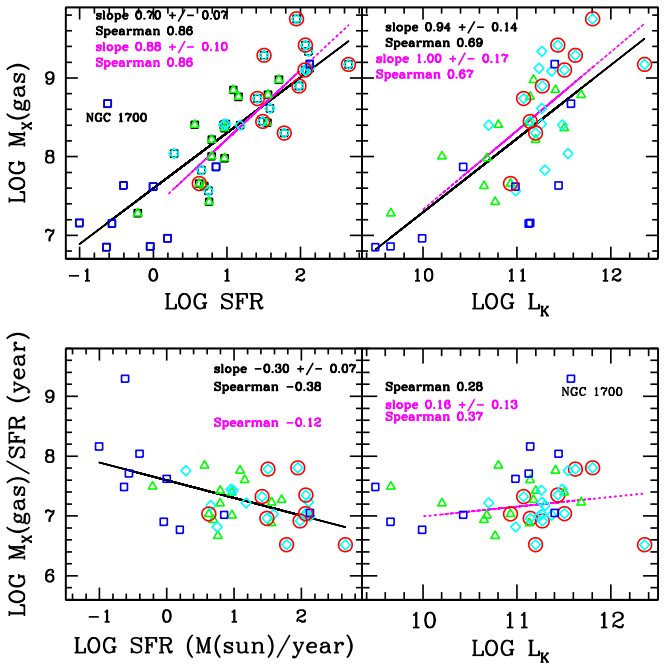

Figure 13. Plots of M_X(gas) vs. SFR (top left), M_X(gas) vs. L_K (top right), M_X(gas)/SFR vs. SFR (bottom left), and M_X(gas)/SFR vs. L_K (bottom right). Systems at merger stages 1 and 2 are marked as open green triangles. Merger stages 3, 4, and 5 are indicated by open cyan diamonds. Merger stages 6 and 7 are identified by blue open squares. Spearman rank correlation coefficients for the full data set are given in black, while the Spearman coefficient for the subset of galaxies with SFR $> 1\ M_\odot\ \mathrm{yr}^{-1}$ are given in magenta. When reliable correlations are seen, the best-fit straight line for the full data set is shown as a solid black line, and for the high-SFR subset as a dashed magenta line. AGN are identified by red circles.

The volume of hot gas is weakly correlated with L_{FIR}/L_K (bottom right panel of Figure 11) and with [3.6]–[24] (Table 5). As noted earlier, both [3.6]–[24] and L_{FIR}/L_K are approximate measures of the sSFR. This correlation may be a consequence of the correlation between volume and SFR, as sSFR tends to increase with increasing SFR for this sample (see Figure 2 and Table 5). NGC 1700 is particularly discrepant in these plots, compared to the other galaxies, with a low sSFR (i.e., low [3.6]–[24] and low L_{FIR}/L_K) and a large volume of hot gas.

In Figure 12, SFR is plotted against $n_e\sqrt{f}$ (upper left panel), F_{60}/F_{100} against $n_e\sqrt{f}$ (upper right panel), SFE with constant CO/H_2 ratio versus $n_e\sqrt{f}$ (middle left), SFE with a variable CO/H_2 ratio versus $n_e\sqrt{f}$ (middle right), and [3.6]–[24] versus $n_e\sqrt{f}$ (lower left). No trends are seen in these five panels.

In the lower right panel of Figure 12, we plot the derived ratio $M_X(\mathrm{gas})/L_X(\mathrm{gas})$ for the 15 galaxies with temperature measurements. The blue solid line on this plot is the relation assuming a constant temperature of 0.3 keV. From the equations given in Section 5, $M_X(\mathrm{gas})/L_X(\mathrm{gas}) = m_P/(\Lambda n_e f)$, so the conversion from L_X(gas) to M_X(gas) is a function of n_e, with $M_X(\mathrm{gas})/L_X(\mathrm{gas}) \propto 1/n_e$ if the temperature and filling factor are constant. The 15 data points lie above the blue line in this plot because they have temperatures higher than 0.3 keV (see Section 6.5), and Λ decreases as temperature increases. The question of the assumed electron temperature is discussed further in Section 6.5.

6.2. M_X(gas)/SFR versus Other Properties

The mass of hot gas is strongly correlated with SFR (Figure 13, upper left). For SFR $> 1\ M_\odot\ \mathrm{yr}^{-1}$, the slope of log M_X(gas) versus log SFR is consistent with one. However, the relationship flattens when lower SFR systems are included, suggesting an excess of hot gas in low-SFR systems. Even when NGC 1700 is excluded, this flattening is seen. We note that the other two galaxies with low SFR and high M_X(gas)/SFR in this figure, NGC 2865 and NGC 5018, both have moderately high K band luminosities (Table 1). As with NGC 1700, virialized gas in the gravitational potential may be contributing to the observed hot gas in these galaxies (see Paper I for detailed discussions of these galaxies). Unfortunately, our sample only has a few systems with low SFR and high L_K, so separating out this additional component to the hot gas is uncertain.

There is also a correlation between M_X(gas) and L_K (Figure 13, upper right). However, this relation has a lower correlation coefficient than M_X(gas) versus SFR. This suggests that the M_X(gas)–L_K relation is a consequence of the SFR–L_K correlation for our sample galaxies, and the hot gas in most of our galaxies is mainly due to SFR rather than older stars.

When both M_X(gas) and SFR are normalized by a tracer of stellar mass, L_K, they still show a strong correlation (Table 5). This indicates that the relation between SFR and M_X(gas) is not simply a richness effect. In contrast, when both M_X(gas) and L_K are normalized by SFR, the correlation is significantly weaker (Table 5). This again implies that M_X(gas) is more closely tied to young stars than to old stars.

The correlation between M_X(gas) and SFR is displayed in another way in the bottom left panel of Figure 13, where we show M_X(gas)/SFR versus SFR. Although a weak anticorrelation is seen for the full sample, once systems with SFR $< 1\ M_\odot\ \mathrm{yr}^{-1}$ are removed, no correlation is seen and the

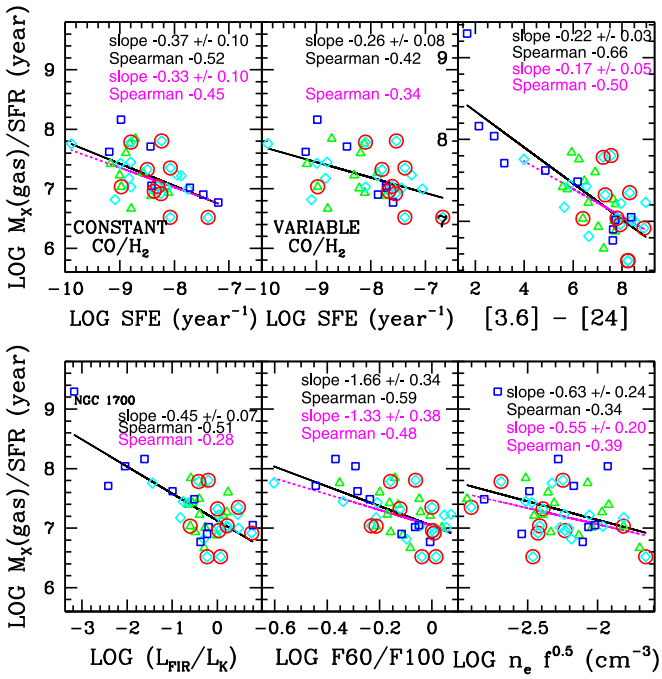

Figure 14. Plots of M_X(gas)/SFR vs. the two estimates of SFE (first and second panels, top row), M_X(gas)/SFR vs. [3.6]–[24] (top right), M_X(gas)/SFR vs. L_{FIR}/F_K (bottom left), M_X(gas)/SFR vs. F_{60}/F_{100} (bottom middle), and M_X(gas)/SFR vs. $n_e\sqrt{f}$ (bottom right). Systems at merger stages 1 and 2 are marked as open green triangles. Merger stages 3, 4, and 5 are indicated by open cyan diamonds. Merger stages 6 and 7 are identified by blue open squares. Spearman rank correlation coefficients for the full data set are given in black, while the Spearman coefficient for the subset of galaxies with SFR $> 1\ M_\odot\ yr^{-1}$ are given in magenta. When reliable correlations are seen, the best-fit straight line for the full data set is shown as a solid black line, and for the high-SFR subset as a dashed magenta line. AGN are identified by red circles.

rms scatter is relatively small (0.37 dex). This is close to the expected scatter based on the uncertainty in M_X(gas) alone, which supports the contention that processes associated with a young stellar population are the main factors responsible for the hot gas in these galaxies, at least when low-SFR systems are excluded.

We plot M_X(gas)/SFR against L_K in the lower right panel of Figure 13. A very weak trend is visible when low-SFR systems are excluded. The postmerger NGC 1700 stands out as having a high M_X(gas)/SFR. After NGC 1700, the next two highest M_X(gas)/SFR galaxies in this plot, NGC 2865 and NGC 5018, are both stage 7 merger remnants with moderately high L_K and low sSFR. In contrast to these three galaxies, galaxies with low K band luminosities ($\leqslant 10^{10}\,L_\odot$) have moderately low M_X(gas)/SFR values, though not extreme. In Paper I, we found that low L_K systems have low L_X(gas)/SFR. Now, we are able to show that M_X(gas)/SFR is also somewhat low for these systems. This may indicate escape of hot gas from lower gravitational fields. However, only a few galaxies fall in this range, so the statistics are very uncertain.

In the upper left and upper middle panels of Figure 14, weak anticorrelations are seen between M_X(gas)/SFR and SFE, but these trends disappear for the variable CO/H_2 ratio when low-SFR systems are not included. The fact that our data set is incomplete in CO makes these conclusions somewhat uncertain.

M_X(gas)/SFR is anticorrelated with the two tracers of sSFR, [3.6]–[24] and L_{FIR}/L_K (Figure 14, upper right and lower left panels, respectively). However, when low-SFR systems are excluded, the trend with [3.6]–[24] weakens and the trend with L_{FIR}/L_K disappears. This again suggests that low sSFR systems sometimes have excess hot gas.

M_X(gas)/SFR is shown to be strongly anticorrelated with F_{60}/F_{100} for the full sample (Figure 14, lower middle panel). This trend is weakened when only the high-SFR sample is included, but is still detected. The cause of this anticorrelation is uncertain; some possible interpretations are discussed in Section 7.2. In addition, a weak anticorrelation is visible between M_X(gas)/SFR and $n_e\sqrt{f}$, particularly when low-SFR systems are omitted (lower right panel Figure 14). In contrast, M_X(gas)/SFR is not correlated with either the volume or the H I-to-H_2 ratio (Table 5).

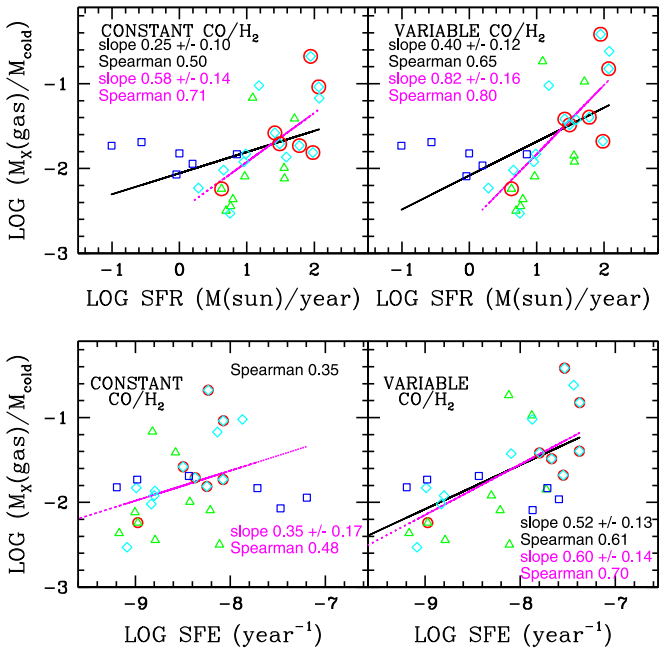

Figure 15. Plots of $M_X(gas)/(M_{H\,I}+M_{H_2})$ vs. SFR (top panels) and SFE (bottom panels). The left column uses a constant CO/H_2 ratio, while the right column uses a variable ratio. Systems at merger stages 1 and 2 are marked as open green triangles. Merger stages 3, 4, and 5 are indicated by open cyan diamonds. Merger stages 6 and 7 are identified by blue open squares. AGN are identified by red circles. Spearman rank correlation coefficients for the full data set are given in black, while the Spearman coefficient for the subset of galaxies with SFR $> 1\ M_\odot\ yr^{-1}$ are given in magenta. When reliable correlations are seen, the best-fit straight line for the full data set is shown as a solid black line, and for the high-SFR subset as a dashed magenta line.

6.3. Ratio of the Mass of Hot Gas to the Mass of Cold Gas versus Other Properties

In Figure 15, the ratio of the mass of hot X-ray-emitting gas to the mass of cold gas ($H\,I + H_2$) is plotted against SFR (top row) and SFE (bottom row). The left panel in each row was calculated using a constant CO/H_2 ratio, while the right panel was calculated with a variable CO/H_2. Figure 15 shows that $M_X(gas)/(M_{H_2}+M_{H\,I})$ increases with increasing SFR, with a better correlation when a variable CO/H_2 ratio is used. A higher Spearman coefficient and a steeper relation are found when the low-SFR systems are omitted. The slope is consistent with one when a variable CO/H_2 ratio is used and low-SFR systems are omitted. The flatter relation when low-SFR systems are included again points to excess M_X(gas) for low-SFR systems.

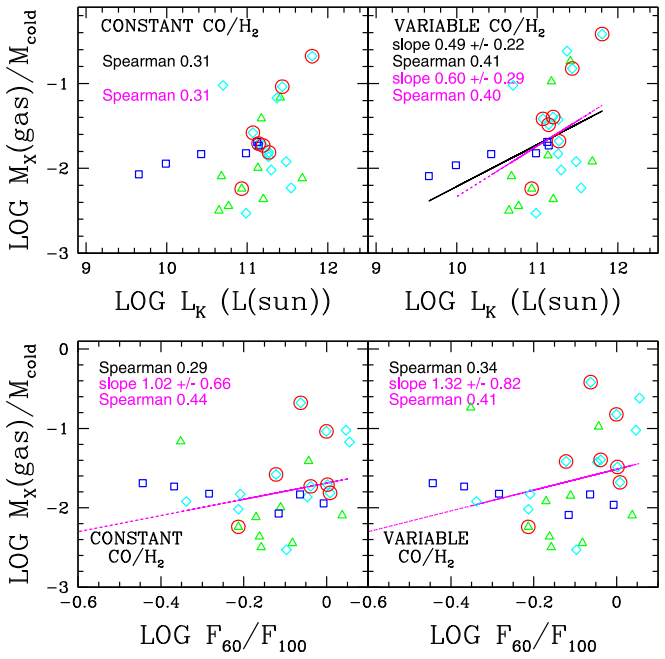

Figure 16. Plots of $M_X(\mathrm{gas})/(M_{\mathrm{H\,I}}+M_{\mathrm{H_2}})$ vs. L_K (top row) and F_{60}/F_{100} (bottom row). The left column uses a constant CO/H_2 ratio, while the right column uses a variable ratio. Systems at merger stages 1 and 2 are marked as open green triangles. Merger stages 3, 4, and 5 are indicated by open cyan diamonds. Merger stages 6 and 7 are identified by blue open squares. AGN are identified by red circles. Spearman rank correlation coefficients for the full data set are given in black, while the Spearman coefficient for the subset of galaxies with SFR $> 1\ M_\odot\ \mathrm{yr}^{-1}$ are given in magenta. When reliable correlations are seen, the best-fit straight line for the full data set is shown as a solid black line, and for the high-SFR subset as a dashed magenta line.

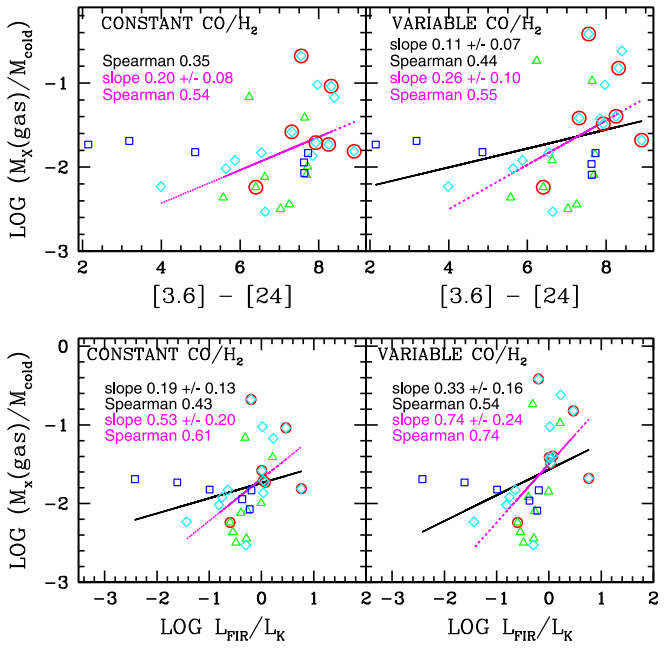

Figure 17. Comparisons between $M_X(\mathrm{gas})/(M_{\mathrm{H\,I}}+M_{\mathrm{H_2}})$ and [3.6]–[24] (top panels), and L_{FIR}/L_K (bottom panels). The best-fit line for the full sample is plotted as a solid black line, while the best-fit line for systems with SFR $> 1.0\ M_\odot\ \mathrm{yr}^{-1}$ is given as a dotted line. The best-fit slope and the Spearman rank correlation coefficient for the full set are shown in black (on top), while the values for the high-SFR subset are shown in magenta (below). Systems at merger stages 1 and 2 are marked as open green triangles. Merger stages 3, 4, and 5 are indicated by open cyan diamonds. Merger stages 6 and 7 are identified by blue open squares. AGN are identified by red circles. NGC 1700 is not plotted. When reliable correlations are seen, the best-fit straight line for the full data set is shown as a solid black line, and for the high-SFR subset as a dashed magenta line. AGN are identified by red circles.

A large amount of scatter is evident in a plot of $M_X(\mathrm{gas})/(M_{\mathrm{H_2}}+M_{\mathrm{H\,I}})$ versus SFE (Figure 15, bottom row), but a reliable correlation is present when a variable CO/H_2 ratio is used. The lack of a full set of CO data makes these results uncertain.

The scatter in $M_X(\mathrm{gas})/(M_{\mathrm{H_2}}+M_{\mathrm{H\,I}})$ may be due in part to variations in the stellar mass. In Figure 16, $M_X(\mathrm{gas})/(M_{\mathrm{H_2}}+M_{\mathrm{H\,I}})$ is plotted against L_K (top panel) and F_{60}/F_{100} (bottom panel). In the left column, the quantities were calculated using a constant CO/H_2 ratio, while the right panel was calculated with a variable CO/H_2. A weak correlation is visible in the upper right panel when low-SFR galaxies are excluded and a variable CO/H_2 ratio is used. The two lowest L_K systems have moderately low $M_X(\mathrm{gas})/(\mathrm{M_{H_2}}+M_{\mathrm{H\,I}})$, and the highest $M_X(\mathrm{gas})/(M_{\mathrm{H_2}}+M_{\mathrm{H\,I}})$ system, NGC 6240, has a very high L_K. In the lower panels of Figure 16, weak correlations between $M_X(\mathrm{gas})/(M_{\mathrm{H_2}}+M_{\mathrm{H\,I}})$, and F_{60}/F_{100} are seen, but only if low-SFR systems are excluded.

Correlations are visible between $M_X(\mathrm{gas})/(M_{\mathrm{H_2}}+M_{\mathrm{H\,I}})$ and our two tracers of sSFR (Figure 17), especially when low-SFR systems are excluded and a variable CO/H_2 ratio is used. The steepening of the slope when low-SFR systems are excluded again signals possible excess of hot gas in low-SFR systems.

6.4. Merger Stage versus Gas Properties

We plot the inferred mass of X-ray-emitting gas $M_X(\mathrm{gas})$ against merger stage in the top left panel of Figure 18. The midmerger stages have higher quantities of hot gas, on average, than the early or late stages. However, this is largely due to the fact that the midmerger galaxies tend to have higher SFRs. When the mass of hot gas is normalized by the SFR (Figure 18, top right), no strong trend is seen. The stage 7 galaxy NGC 1700 stands out as having a high $M_X(\mathrm{gas})/\mathrm{SFR}$. The next two highest $M_X(\mathrm{gas})/\mathrm{SFR}$ systems, the stage 7 galaxies NGC 2865 and NGC 5018, also have low sSFR.

The bottom row of Figure 18 compares the merger stage with the ratio of hot gas to cold gas $M_X(\mathrm{gas})/(M_{\mathrm{H_2}}+M_{\mathrm{H\,I}})$, using the standard Galactic CO/H_2 ratio (left panel) or the variable CO/H_2 ratio (right panel). Stages 3 and 4 tend to have proportionally more hot gas. This is likely a consequence of the fact that galaxies in those stages tend to have higher SFRs. Because of the inhomogeneity of the sample, the small number of systems in each merger stage, and the lack of a full set of CO data, trends with merger stage in our sample are uncertain. In these plots, the galaxy with the highest $M_X(\mathrm{gas})/(M_{\mathrm{H_2}}+M_{\mathrm{H\,I}})$ is NGC 6240. NGC 1700 is not plotted in the bottom row of Figure 18, because it lacks a full set of CO data.

6.5. Gas Temperature

As mentioned earlier, our derivations of electron density and $M_X(\mathrm{gas})$ depend upon the assumed temperature, and temperatures are available for only 15 of our sample galaxies from the X-ray spectra (see Paper I). For the remaining galaxies, we assumed a constant temperature of 0.3 keV. For comparison, kT ranges from 0.37 to 1.0keV for the 15 systems for which temperatures are available in Paper I. In some cases, we were able to use a two-temperature model for the hot gas; in those cases, we used the luminosity-weighted temperature in the subsequent analysis. For comparison, Mineo et al. (2012b) found lower temperatures on average for their sample galaxies

(mean of 0.24 keV for single-temperature models). The derived temperatures depend upon the assumptions used in modeling the X-ray spectrum, including how the power-law component is modeled, so they are somewhat uncertain (see Paper I). Because our sample is an archive-selected sample, there is a selection bias in the subset of galaxies with derived temperatures. Compared to the galaxies in the sample without measured temperatures, the galaxies with temperatures tend to have longer, more sensitive exposures, and they tend to be more extreme systems with higher luminosities. In contrast, the Mineo et al. (2012b) sample, with lower temperatures on average, contains more normal spiral galaxies and irregulars as well as some mergers. We therefore assume the more modest temperature of 0.3 keV for our galaxies without temperature measurements, assuming that they are less extreme than the other systems. However, this is quite uncertain.

To test whether our conclusions are affected by our assumption of 0.3 keV for the galaxies without derived temperatures, we reran our correlation analysis with four alternative assumptions. First, we reran the analysis using a constant $kT = 0.3$ keV for all the galaxies, even those for which we have a direct measure of the temperature. Second, we did the calculations assuming a constant $kT = 0.6$ keV for all galaxies.

Third, we reran the analysis assuming that the temperature is correlated with SFR. In Paper I, we did not find any correlation of temperature with SFR. Mineo et al. (2012b) also did not find a correlation between temperature and SFR for their sample of star-forming galaxies. However, Grimes et al. (2005) noted that the ULIRGs in their sample tend to have higher temperatures, up to about 0.8 keV. Therefore, as a limiting case to investigate how temperature may potentially affect our results, we assume that $\log T_X$ increases linearly with $\log$ SFR, and we set $kT = 0.2$ keV for the systems with the lowest SFRs ($0.1\,M_\odot\,\mathrm{yr}^{-1}$), increasing to 1.0 keV for systems with SFR $= 100\,M_\odot\,\mathrm{yr}^{-1}$.

As a fourth test, we investigated how our results changed if we assumed that the temperature depends upon L_X(gas) rather than on SFR. In contrast to actively star-forming galaxies, ellipticals show a steep relation between L_X(gas) and temperature of $L_X(\mathrm{gas}) \propto T_X^{4.5}$ (Goulding et al. 2016). As a limiting case, we assumed that $L_X(\mathrm{gas}) \propto T_X^{4.5}$, as found for ellipticals (Goulding et al. 2016). Assuming a temperature of 0.2 keV for the galaxies with the lowest L_X(gas) in our sample, this gives 1.0 keV for the highest L_X(gas) system. This is a more extreme range than typically found for star-forming galaxies, ergo it is a limiting case.

For each of the above cases, we also explored how our results change when we included a correction from the observed 0.3–8.0 keV L_X(gas) to the bolometric luminosity of the gas, including light outside the 0.3–8.0 keV *Chandra* window. This conversion is a function of temperature. Using the PIMMS[12] software, we find that $L_{\mathrm{bol}}(\mathrm{gas})/L_X(\mathrm{gas})$(0.3–8.0 keV) drops from 2.39 at 0.3 keV to 1.39 at 1.0 keV.

In rerunning the correlation analysis, we find that the basic conclusions of this paper do not change dramatically with these different assumptions about the temperature. The Spearman coefficients and the best-fit relations change slightly with different assumptions about the temperature, but the basic conclusions remain the same. For a few of the relations that have correlation coefficients near our "weak"/"none" boundary or our "strong"/"weak" boundary, small changes in the correlation coefficient may reclassify the relation. The most notable case is the very weak correlation between $M_X(\mathrm{gas})/\mathrm{SFR}$ and L_K, which drops below the cutoff for a "weak" correlation for some of these alternative cases, but increases slightly in significance for the linear $\log(T_X)$–$\log(\mathrm{SFR})$ case including the correction for light outside of the *Chandra* bandpass. This emphasizes that the $M_X(\mathrm{gas})/\mathrm{SFR}$–$L_K$ correlation is very marginal, and more data is needed to confirm or refute it.

For most of the relations discussed above, however, although the correlation coefficients change slightly with different assumptions about the temperatures, the classification of the relation does not change. Thus, the conclusions of this paper are not strongly influenced by our lack of temperature measurements.

[12] Portable, Interactive, Multi-Mission Simulator; http://asc.harvard.edu/toolkit/pimms.jsp.

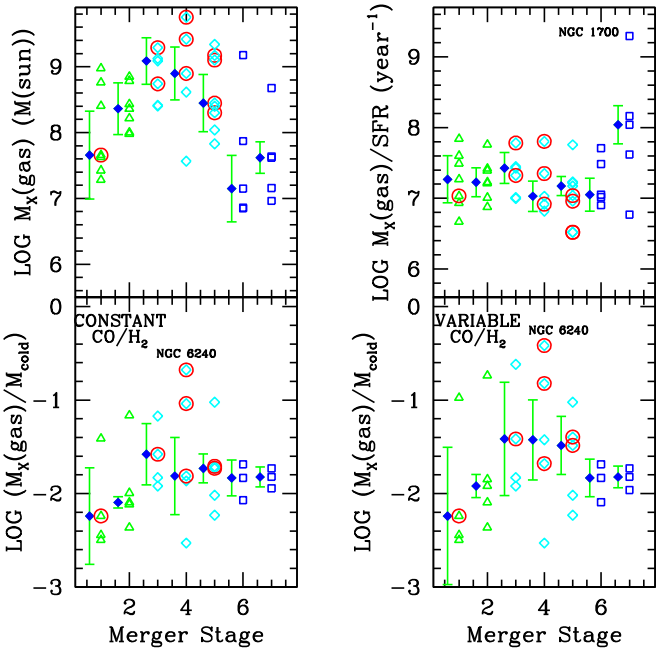

Figure 18. Top left: hot gas mass M_X(gas) vs. merger stage. Top right: $M_X(\mathrm{gas})/\mathrm{SFR}$ vs. merger stage. Bottom row: $M_X(\mathrm{gas})/M_{\mathrm{cold}} = M_X(\mathrm{gas})/(M_{H_2} + M_{H\,I})$, calculated with a constant CO/H_2 ratio (left panel) and the variable CO/H_2 ratio (right panel). Systems at merger stages 1 and 2 are marked as open green triangles. Merger stages 3, 4, and 5 are indicated by open cyan diamonds. Merger stages 6 and 7 are identified by blue open squares. AGN are identified by red circles. NGC 1700 is not plotted in the bottom panels, due to the lack of a complete set of CO data. The filled blue diamonds are the median values for each stage, slightly offset to the left. The error bars plotted on the median values display the semi-interquartile range, equal to half the difference between the 75th percentile and the 25th percentile.

7. Discussion

We calculated the volume, mass, and electron density of the hot X-ray-emitting gas in our sample galaxies, and compared with other properties of the galaxies, including the SFR, L_K, the mass of cold gas, and the SFE. We have searched for correlations between a large number of variables, and discovered several new correlations and anticorrelations in our data. These, and many apparent noncorrelations, are listed in Table 5.

7.1. Volume and M_X(gas) vs. SFR and L_K

Some of the most important correlations are:

(1) The volume of hot gas increases as the SFR goes up, with a high correlation coefficient (Figure 9). When galaxies

with SFR $< 1\ M_{\odot}\ \mathrm{yr}^{-1}$ are excluded, the slope of the best-fit log volume-log SFR line is 0.97 ± 0.15 (Figure 9). Including low-SFR systems flattens this relation.

(2) The volume of hot gas is also correlated with L_{K}, but with a smaller correlation coefficient (Figure 11).

(3) The volume of hot gas also correlates with SFE, $L_{\mathrm{FIR}}/L_{\mathrm{K}}$, and [3.6]–[24], but only weakly (Figures 10 and 11, and Table 5).

(4) There is a strong correlation between M_{X}(gas) and SFR (Figure 13). The slope of the log–log plot is 0.88 ± 0.10 when low-SFR galaxies are excluded, consistent with a simple $M_{\mathrm{X}}(\mathrm{gas}) \propto \mathrm{SFR}$ relation. This relation flattens when low-SFR systems are included.

(5) There is a correlation between M_{X}(gas) and L_{K} (Figure 13), but with a lower correlation coefficient than M_{X}(gas) and SFR.

(6) As the SFR increases, $M_{\mathrm{X}}(\mathrm{gas})/(M_{\mathrm{H_2}} + M_{\mathrm{H\,I}})$ goes up (Figure 15), especially when a variable $\mathrm{CO}/\mathrm{H_2}$ ratio is used and low-SFR systems are excluded. For the latter case, the correlation is strong and the slope of the log–log plot is consistent with one.

(7) There is a weak correlation between $M_{\mathrm{X}}(\mathrm{gas})/(M_{\mathrm{H_2}} + M_{\mathrm{H\,I}})$ and L_{K} when a variable $\mathrm{CO}/\mathrm{H_2}$ ratio is used (Figure 16).

(8) There is a trend of increasing $M_{\mathrm{X}}(\mathrm{gas})/(M_{\mathrm{H_2}} + M_{\mathrm{H\,I}})$ ratio with increasing SFE, especially when a variable $\mathrm{CO}/\mathrm{H_2}$ ratio is used (Figure 15). This trend is weaker than the relation with SFR.

(9) There is a weak correlation between $M_{\mathrm{X}}(\mathrm{gas})/(M_{\mathrm{H_2}} + M_{\mathrm{H\,I}})$ and F_{60}/F_{100} (Figure 16).

For high-SFR systems, the linear relations between volume and SFR—and between M_{X}(gas) and SFR—can be explained in a straightforward manner: a larger SFR means more supernovae and more stellar winds, which produce a larger volume of hot gas and a larger M_{X}(gas). For galaxies with SFR $> 1\ M_{\odot}\ \mathrm{yr}^{-1}$, hot gas associated with star formation dominates M_{X}(gas), and any contribution from processes associated with the older stellar population is negligible. However, for galaxies with lower SFRs and high K band luminosities (and therefore low sSFRs) we find evidence for excess hot gas relative to the linear $M_{\mathrm{X}}(\mathrm{gas})-\mathrm{SFR}$ relation. This may be due to contributions to the X-ray-emitting hot gas from other sources, perhaps mass loss from older stars that has been virialized in the gravitational potential.

The weaker correlation between volume and SFE compared to volume versus SFR is accounted for by the fact that some high-SFE systems have only moderate SFRs, and it is the SFR that controls the number of supernovae and the amount of stellar wind, not the SFE. The weakness of the correlation between volume and the sSFR as measured by [3.6]–[24] and $L_{\mathrm{FIR}}/L_{\mathrm{K}}$ may be explained in a similar manner.

The correlations between L_{K} and the hot gas mass—and between L_{K} and the volume of hot gas—may be indirect results of the correlation between SFR and L_{K}. The SFR-L_{K} correlation, in turn, is a consequence of the fact that most of the galaxies in our sample are star-forming galaxies on the galaxy main sequence. Because the volume$-L_{\mathrm{K}}$ and $M_{\mathrm{X}}(\mathrm{gas})-L_{\mathrm{K}}$ correlations are weaker than the volume$-$SFR and M_{X}(gas)–SFR correlations, we conclude that star formation is more directly responsible for the hot gas, not the older stellar population.

The strong correlation between the hot-to-cold gas mass ratio and the SFR, in contrast to the weak correlation between the hot-to-cold gas mass ratio and L_{K}, confirms that the younger stellar population is primarily responsible for the hot gas, not older stars. The amount of hot gas in our galaxies is small compared to the amount of colder gas (see Table 2), so conversion of colder material into hot gas noticeably affects the numerator in $M_{\mathrm{X}}(\mathrm{gas})/(M_{\mathrm{H_2}} + M_{\mathrm{H\,I}})$, but not the denominator. The higher the SFR, the more hot gas that is produced. Thus, the $M_{\mathrm{X}}(\mathrm{gas})/(M_{\mathrm{H_2}} + M_{\mathrm{H\,I}})$ ratio is directly correlated with the SFR. The linear log $M_{\mathrm{X}}(\mathrm{gas})/(M_{\mathrm{H_2}} + M_{\mathrm{H\,I}})$ versus log SFR relation for high-SFR systems provides additional support for the idea that the hot gas is mainly due to young stars in these galaxies. The flattening of this relation at lower SFR again indicates excess hot gas in low-SFR, low-sSFR systems.

The strong correlation between $M_{\mathrm{X}}(\mathrm{gas})/(M_{\mathrm{H_2}} + M_{\mathrm{H\,I}})$ and SFR is consistent with the recent Moreno et al. (2019) simulations of star formation and feedback in galaxy mergers, in which they investigate the relative amounts of hot, warm, cool, and cold gas. In their models, the interaction causes an increase in the amount of cold, ultradense interstellar gas by a factor of about 2.4 on average. This, in turn, enhances the SFR. The amount of hot gas increases during the starburst (by about 400%), while the total amount of cold and warm gas mass decreases only slightly or remains constant. The net effect would be an increase in $M_{\mathrm{X}}(\mathrm{gas})/(M_{\mathrm{H_2}} + M_{\mathrm{H\,I}})$ during the burst, consistent with our correlation with SFR. In the Moreno et al. (2019) models, the hot gas is produced solely by stellar/supernovae feedback; they do not include AGN feedback or a pre-existing hot halo.

The larger scatter in the $M_{\mathrm{X}}(\mathrm{gas})/(M_{\mathrm{H_2}} + M_{\mathrm{H\,I}})$ versus SFE correlation and its weaker correlation compared to $M_{\mathrm{X}}(\mathrm{gas})/(M_{\mathrm{H_2}} + M_{\mathrm{H\,I}})$ versus SFR is likely due to some low-SFR systems having high SFEs; it is the SFR that directly controls the amount of hot gas rather than the SFE.

The weak trend of increasing $M_{\mathrm{X}}(\mathrm{gas})/(M_{\mathrm{H_2}} + M_{\mathrm{H\,I}})$ with increasing F_{60}/F_{100} ratio may be another indirect consequence of the $M_{\mathrm{X}}(\mathrm{gas})/(M_{\mathrm{H_2}} + M_{\mathrm{H\,I}})$ versus SFR correlation. Because F_{60}/F_{100} increases with SFR on average for our sample galaxies (Figure 2), galaxies with higher $M_{\mathrm{X}}(\mathrm{gas})/(M_{\mathrm{H_2}} + M_{\mathrm{H\,I}})$ and SFR tend to have larger F_{60}/F_{100}.

Another factor that may affect M_{X}(gas) is escape of hot gas from the gravitational field of the galaxy, particularly in low-mass systems. Our data shows a hint of lower $M_{\mathrm{X}}(\mathrm{gas})/\mathrm{SFR}$ for low-L_{K} systems (Figure 13). However, this is uncertain because our sample only includes a few low-mass systems. The majority of galaxies in our sample lie in only a small range of L_{K} ($10^{10}\,L_{\odot}$–$10^{11.5}\,L_{\odot}$), so it is difficult to find trends with L_{K} in our sample. Low-mass galaxies may have lower ratios of baryonic mass M_{baryon} to dynamical mass M_{dyn} compared to high-mass systems (e.g., Côté et al. 2000; Torres-Flores et al. 2011). The lower $M_{\mathrm{baryon}}/M_{\mathrm{dyn}}$ in low-mass systems has been attributed to either mass loss from galactic winds (e.g., van den Bosch 2000; Brook et al. 2012) or less efficient infall into lower-mass dark halos (e.g., Sales et al. 2017). A deficiency in hot gas in low-mass systems, if confirmed, may point to increased escape of baryons via winds. A larger *Chandra* imaging survey including more low-mass systems would be helpful to better characterize $M_{\mathrm{X}}(\mathrm{gas})/\mathrm{SFR}$ and the scatter in this ratio for low-mass galaxies.

To search for additional evidence that the hot gas content in our sample galaxies is affected by the mass and/or the older

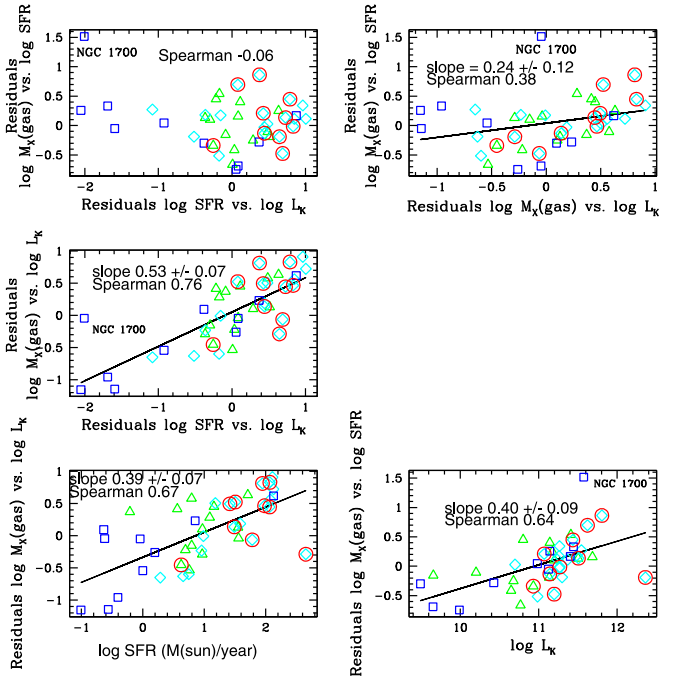

Figure 19. A search for correlations between residuals of best-fit plots for various quantities. Residuals are defined as observed—(best-fit value), i.e., a negative residual in the log SFR vs. log L_K plot means that it has a low SFR relative to L_K (that is, a low sSFR or "post-starburst"). Systems at merger stages 1 and 2 are marked as open green triangles. Merger stages 3, 4, and 5 are indicated by open cyan diamonds. Merger stages 6 and 7 are identified by blue open squares. AGN are identified by red circles.

stellar population in addition to the SFR, we calculated the residuals from the best-fit linear relations for log SFR versus log L_K, log M_X(gas) versus log SFR, and log M_X(gas) versus log L_K. We then searched for correlations between these residuals (top three panels in Figure 19). Strong correlations between these residuals might suggest the existence of a "fundamental plane" of M_X(gas) versus log SFR versus log L_K.

A weak correlation is seen between the residuals of log M_X(gas) versus SFR and those of M_X(gas) versus L_K (Figure 19, upper right). A strong correlation is seen between the residuals of log M_X(gas) versus log L_K and those of log SFR versus log L_K (Figure 19, left panel, middle row). The most discrepant galaxies in this plot are NGC 5018, NGC 2865, and Arp 222 (the three stage 7 mergers in the lower left corner). All of these were identified in Paper I as post-starbursts, and all have low sSFR (i.e., have large negative residuals in the log SFR versus log L_K relation). They also have large negative residuals compared to the best-fit log M_X(gas) versus log L_K relation. What is discrepant about these galaxies is their K band luminosities, which are high relative to their SFRs. Figure 19 shows that NGC 1700 has a high relative M_X(gas) compared to these other low-sSFR galaxies.

In the bottom row of Figure 19, we also compared these residuals with L_K and the SFR. There is a positive correlation between the residuals of the M_X(gas) versus L_K relation and the SFR (Figure 19, bottom left). Galaxies with low SFRs tend to be deficient in M_X(gas) compared to the M_X(gas) versus L_K relation. That is because they also tend to have low sSFRs, and it is the SFR that determines the mass of hot gas, not L_K. The galaxies in the lower corner of that plot have low SFRs compared to their K band luminosities, and therefore they have low M_X(gas) compared to their L_K.

We also see a positive correlation between the residuals of the M_X(gas) versus SFR relation and L_K (Figure 19, bottom right panel). NGC 1700 stands out as having excess hot gas, while systems with low K band luminosities tend to have less hot gas relative to the M_X(gas) versus SFR relation. This suggests that some gas may have been lost from these systems. Unfortunately, our sample only contains a few galaxies with low K band luminosities and/or low sSFR, so this result is uncertain.

We conclude that only a few galaxies in our sample deviate from a straight line in the log M_X(gas)–log SFR–log L_K plane. To better understand these deviations, it would be helpful to increase the number of post-starburst galaxies in our sample, as well as the number of low-mass galaxies.

7.2. *Trends with* M_X*(gas)/SFR and* $n_e\sqrt{f}$

In addition to the strong positive correlations discussed above, some weak anticorrelations are also seen in the data:

(1) There are weak anticorrelations between M_X(gas)/SFR and F_{60}/F_{100}, and between M_X(gas)/SFR and [3.6]–[24] (Figure 14). These anticorrelations hold even when low-SFR systems are excluded.
(2) As M_X/SFR goes up, $n_e\sqrt{f}$ goes down, even when low-SFR systems are excluded (Figure 14). This is also a weak trend.
(3) There is a weak trend of decreasing volume with increasing $n_e\sqrt{f}$ (Figure 11).

Some parameters are neither correlated or anticorrelated:

(4) There is no correlation of M_X(gas)/SFR with SFR, if low-SFR systems are excluded (Figure 13). There is no correlation with M_X(gas)/SFR for a variable CO/H_2 ratio (Figure 14).
(5) The SFR, [3.6]–[24], and F_{60}/F_{100} do not correlate with $n_e\sqrt{f}$ (Figure 12).
(6) No significant correlations are found between M_X(gas)/SFR and volume (Table 5), nor is any correlation found between M_X(gas)/SFR and L_{FIR}/L_K when low-SFR systems are excluded (Figure 14).

Although M_X(gas)/SFR is anticorrelated with F_{60}/F_{100} and with [3.6]–24], M_X(gas)/SFR is not correlated (either positively or negatively) with SFR, in spite of the fact that F_{60}/F_{100} and [3.6]–[24] are both (weakly) correlated with SFR. Furthermore, although volume and $n_e\sqrt{f}$ are weakly anticorrelated, and SFR is correlated with volume, $n_e\sqrt{f}$ is not correlated with SFR.

These results suggest that another factor, aside from SFR, contributes to the observed variations in M_X(gas)/SFR and $n_e\sqrt{f}$. One possibility is differences in timescale: variations in the age of an ongoing starburst or the time since the end of a starburst may affect $n_e\sqrt{f}$ and M_X(gas)/SFR, as well as other parameters of the system. Numerical simulations show that interaction-triggered starbursts can last for extended periods ($\geqslant$100 Myr; Lotz et al. 2000; Di Matteo et al. 2008; Bournaud et al. 2011; Fensch et al. 2017). This timescale is similar to the radiative cooling times for the gas (median of 60 Myr; see Section 5), as well as to the timescale over which the UV data is measuring the SFR ($\sim$100 Myr; Kennicutt & Evans 2012). If the cooling time is less than the timescale over which the SFR is measured, and if the cooling time is less than the age of the

burst, then the M_X(gas)/SFR may decrease late in a burst (i.e., some hot gas has cooled, but the UV-bright stars contributing to our SFR estimate have not yet died). The sSFR as measured by [3.6]–[24] and L_{FIR}/L_K may also vary with time during a burst. Presumably, the electron density and/or filling factor also evolve with time during a burst, along with F_{60}/F_{100}, the volume of hot gas, and M_X(gas)/SFR. Further theoretical modeling is needed to better understand the relationships between these parameters in evolving starbursts.

A second factor that may contribute to variations in M_X(gas)/SFR and $n_e\sqrt{f}$ is the efficiency of early feedback. According to numerical simulations, stellar winds and radiation pressure early in a starburst disrupt molecular clouds, making it easier for subsequent supernovae to produce hot gas (Hopkins et al. 2012a, 2013b; Agertz et al. 2013). The efficiency of early feedback might be related to the spatial density of star formation; more concentrated distributions of young stars may have more early UV radiation per volume, allowing quicker destruction of molecular gas. This may lead to easier escape for hot gas from the region, and thus less diffuse X-ray emission. More concentrated distributions of young stars would presumably lead to more intense UV interstellar radiation fields and therefore hotter dust and higher F_{60}/F_{100} ratios (e.g., Desert et al. 1990). The F_{60}/F_{100} ratio is weakly anticorrelated with M_X(gas)/SFR, consistent with this scenario. The [3.6]–[24] color may also increase with higher spatial concentrations of young stars, and [3.6]–[24] is also weakly anticorrelated with M_X(gas)/SFR. Further study is needed to investigate how all of these parameters vary with the density of OB stars in a galaxy.

A third factor that might affect M_X(gas)/SFR is the initial mass function (IMF). A top-heavy IMF may lead to an increase in supernovae compared to lower-mass stars, which might produce a larger M_X(gas)/SFR when the SFR is derived from the UV continuum. It has been suggested that high-SFR and/or high-SFE galaxies may have IMFs skewed to high-mass stars (Rieke et al. 1980; Elbaz et al. 1995; Brassington et al. 2007; Köppen et al. 2007; Weider et al. 2013; Brown & Wilson 2019). Thus, one might expect higher M_X(gas)/SFR for systems with higher SFR or higher SFE. However, we do not see a correlation between M_X(gas)/SFR and SFR, nor between M_X(gas)/SFR and SFE. This means that either IMF variations are not responsible for the spread in M_X(gas)/SFR or the IMF is not correlated with SFR or SFE.

Another factor that might affect M_X(gas)/SFR and $n_e\sqrt{f}$ is metallicity. A number of studies have concluded that the SFR of star-forming galaxies depends upon metallicity in addition to stellar mass; for the same stellar mass, lower-metallicity systems have higher SFRs (Ellison et al. 2008; Lara-López et al. 2010; Mannucci et al. 2010; Hirschauer et al. 2018, but see Izotov et al. 2014, 2015). This result has been explained by infall of low-metallicity gas, fueling star formation. Our M_X(gas)/SFR values may be artificially skewed by metallicity, as the value of L_X(gas) that is derived from the *Chandra* spectra is affected by metallicity (see Paper I). In addition, the fraction of the supernovae and stellar wind energy converted into X-ray flux may be a function of metallicity. A larger sample of galaxies, including more low-metallicity systems, would be helpful to investigate this issue further.

Unfortunately, we do not have a measure of the volume filling factor of the hot gas, f, independently of n_e, to determine whether f varies significantly from system to system. Based on theoretical arguments and/or hydrodynamical simulations, for a range of systems, f has variously been estimated to be 70–80% (McKee & Cowie 1977), 20–40% (Breitschwerdt et al. 2012), 30–40% (Kim & Ostriker 2017), or anywhere between 10 and 90% depending upon the supernovae rate and the average gas density (Li et al. 2015). In general, according to simulations, the higher the density of star formation, the larger the expected hot gas filling factor (Breitschwerdt et al. 2012; Li et al. 2015). One might expect higher SFRs to produce faster winds, as has been found for the warm ionized medium (e.g., Heckman et al. 2015). A faster wind may lead to lower n_e values. If the filling factor increases with SFR but n_e decreases, this might explain the lack of a trend between $n_e\sqrt{f}$ and SFR. Independent determinations of n_e and f (e.g., Kregenow et al. 2006; Jo et al. 2019) are needed to test this possibility.

7.3. The Scatter in M_X(gas)

One of the major conclusions of the current paper is that, excluding low-SFR systems, M_X(gas)/SFR is constant with SFR with an rms spread of only 0.34 dex. A number of factors may contribute to this scatter, in addition to age, metallicity, or IMF differences. First, as discussed in Section 5, the decomposition of the X-ray spectrum into a thermal and a nonthermal component introduces some uncertainty to our determination of L_X(gas) (see Paper I). Second, as also discussed in Section 5, the unknown extent of the hot gas along our line of sight leads to uncertainties in the volume of the hot gas, which contributes to the scatter in the parameters derived from the volume. Systematic variations in the geometry of the hot gas may further affect the observed relations. For example, systems with lower SFR may have disk-like distributions of cold gas, with coronal gas extending out of the galactic plane, while higher-SFR systems, which are more likely to be in the midst of a merger, may have gas distributions that are more spherical. System-to-system variations in the gravitational masses of the galaxies, which likely affect outflow rates and potential loss of hot gas, may be another factor contributing to the scatter. We found that galaxies with low K band luminosities tend to have lower M_X(gas)/SFR ratios compared to other galaxies (Figure 16), suggesting that low-mass galaxies may lose some hot gas. The large-scale environment may also affect the M_X(gas)/SFR ratio, however, L_X(gas)/SFR is not correlated with local galaxy density (Paper I); M_X(gas)/SFR and M_X(gas)/(M_{H_2}+$M_{H\,I}$) are also not correlated with local galaxy density. Another factor that may contribute to the observed scatter in these plots is our assumption of a temperature of $kT = 0.3$ keV for the hot gas in the systems without an X-ray determination of temperature. Longer *Chandra* exposures would be useful to spectroscopically determine the temperature of the gas in more of the galaxies.

7.4. NGC 1700

As noted several times in this paper, the late-stage merger NGC 1700 does not fit some of the strong relations seen in this study. NGC 1700 has a large X-ray size relative to its SFR. It also has a high X-ray luminosity and a large mass of hot X-ray-emitting gas. This suggests that either NGC 1700 is in a special evolutionary state compared to the other systems in our sample,

or it acquired its hot gas via a different process. Maybe NGC 1700 was a pre-existing elliptical that already had a large amount of hot gas, which then swallowed a gas-rich galaxy. It is sometimes difficult to distinguish between the remnant of a spiral–spiral merger and the remnant of an elliptical-spiral merger. In appearance, NGC 1700 is an elliptical-like galaxy surrounded by tidal debris, but its merger history is uncertain. It was classified as the remnant of a spiral–spiral major merger by Schweizer & Seitzer (1992) and Brown et al. (2000), but Statler et al. (1996) and Kleineberg et al. (2011) conclude that it is the result of the merger of at least three galaxies—two large spirals and a third smaller galaxy. If NGC 1700 is the product of a single major merger, perhaps it is in a later stage in the conversion from a major merger to an elliptical than the other postmerger galaxies in our sample. Theory suggests that ellipticals produced by major mergers can build a large quantity of hot gas via the virialization of gas lost from red giants in the gravitational potential well, with possible heating by Type Ia supernovae and/or AGN feedback (Ciotti et al. 1991, 2017; Pellegrini & Ciotti 1998; Mathews & Brighenti 2003). This process is expected to be very slow, with timescales of many gigayears. Expanding our sample to include more galaxies like NGC 1700 would be helpful to better understand how hot gas grows in such systems. More generally, increasing the number of low-sSFR galaxies in our sample is needed to investigate how the hot gas in galaxies evolves as star formation fades in a quenched or quenching galaxy.

8. Summary

We have measured the spatial extent of the hot interstellar gas in a sample of 49 interacting and merging galaxies in the nearby universe. For systems with SFR $> 1\,M_{\odot}\,\mathrm{yr}$, we found strong near-linear correlations between the volume of hot gas and the SFR, as well as between $M_{\rm X}$(gas) and SFR. This supports the idea that supernovae and stellar winds are responsible for the hot gas. As expected, the $M_{\rm X}(\mathrm{gas})/(M_{\rm H_2} + M_{\rm H\,I})$ ratio also increases linearly with increasing SFR for high-SFR systems. These results are consistent with recent hydrodynamical simulations of interactions including feedback.

In low-SFR, low-sSFR systems, we find evidence for an excess of hot gas relative to the relations for higher-SFR systems. This excess may be associated with mass loss from older stars. However, our sample only includes a few galaxies with low sSFR rates, so this result is uncertain. In addition, we see a possible deficit of hot gas in low-mass systems, perhaps due to escape from the gravitational field of the galaxy. However, this result is also uncertain, due to the small number of low-mass systems in our sample.

The $M_{\rm X}(\mathrm{gas})/\mathrm{SFR}$ is weakly anticorrelated with F_{60}/F_{100}, [3.6]–[24], and $n_{\rm e}\sqrt{f}$. The inferred electron density decreases with increasing volume of hot gas assuming a constant filling factor. These results may be a consequence of variations in the spatial density of young stars, the age of the stars, the metallicity, the IMF, and/or the efficiency of feedback in these galaxies.

We thank the anonymous referee for very helpful suggestions which greatly improved this paper. This research was supported by NASA *Chandra* archive grant AR6-17009X, issued by the Chandra X-ray Observatory Center, which is operated by the Smithsonian Astrophysical Observatory for and on behalf of NASA under contract NAS8-03060. Support was also provided by National Science Foundation Extragalactic Astronomy grant ASTR-1714491. The scientific results reported in this article are based on data obtained from the *Chandra* Data Archive. This research has also made use of the NASA/IPAC Extragalactic Database (NED), which is operated by the Jet Propulsion Laboratory, California Institute of Technology, under contract with NASA. This work also utilizes archival data from the *Spitzer Space Telescope*, which is operated by the Jet Propulsion Laboratory, California Institute of Technology, under a contract with NASA. This study also uses archival data from the NASA *Galaxy Evolution Explorer* (*GALEX*), which was operated for NASA by the California Institute of Technology under NASA contract NAS5-98034.

Appendix
Chandra 0.3–1.0 keV Maps

For the 44 systems for which we can measure X-ray radial profiles, the unsmoothed *Chandra* 0.3–1.0 keV maps are displayed in the right panels of Figures 20–27. When only one *Chandra* data set is available for the galaxy, the *ciao* command *fluximage* was used to convert into units of photons $\mathrm{s^{-1}\,cm^{-2}\,arcsec^{-2}}$, using an exposure-correction map with a 0.8 keV effective energy. When multiple *Chandra* data sets are available for one system, the data sets have been merged together using the *ciao* command *merge_obs*, which also does the exposure correction and flux calibration. The left panels of Figures 20–27 show either the SDSS *g* band image (when available) or the *GALEX* NUV image. Contours of the X-ray surface brightness are overlaid on the *Chandra* images. These have been lightly smoothed using the ds9 software,[13] with the smooth parameter set to 6.

[13] SAOImageDS9 development has been made possible by funding from the *Chandra* X-ray Science Center (CXC) and the High Energy Astrophysics Science Archive Center (HEASARC), with additional funding from the *JWST* Mission office at the Space Telescope Science Institute.

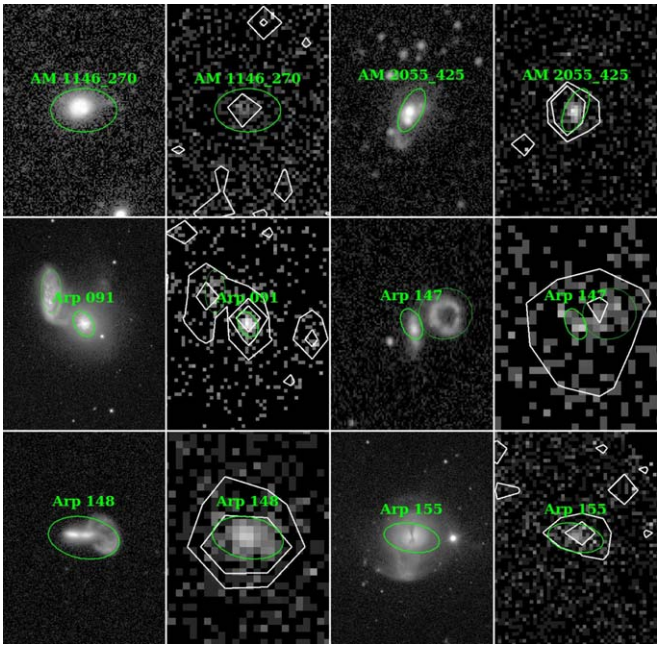

Figure 20. Montage of images of the galaxies. The left panel is either the SDSS g image or the *GALEX* NUV image (if no SDSS images exist). The right panel is the unsmoothed exposure-corrected *Chandra* 0.3–1.0 keV low-energy map. Logarithmic contours are overlaid in white on the *Chandra* image, with units of (3.0, 7.6, 33.5, 178, and 1000) $\times$ 10^{-9} photons s^{-1} cm^{-2} $arcsec^{-2}$. The final best-fit ellipse(s) are overlaid in green on both plots.

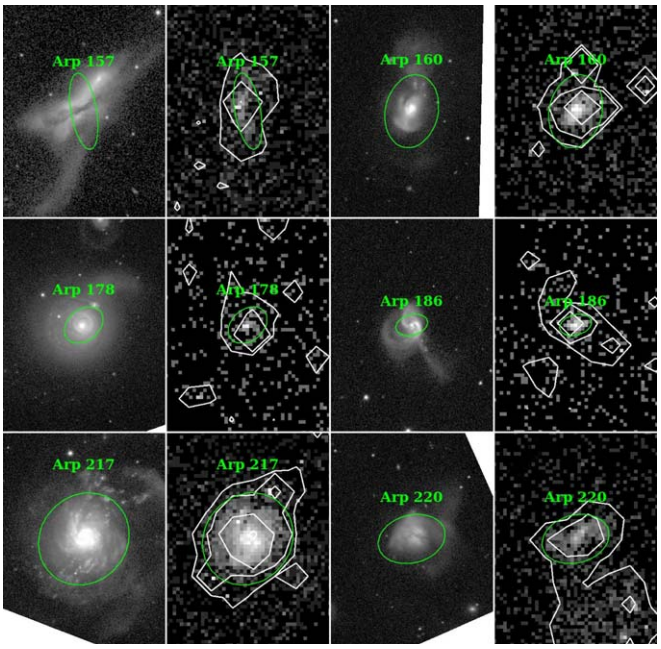

Figure 21. Montage of images of the galaxies. The left panel is either the SDSS g image or the *GALEX* NUV image (if no SDSS images exist). The right panel is the unsmoothed exposure-corrected *Chandra* 0.3–1.0 keV low-energy map. Logarithmic contours are overlaid in white on the *Chandra* image, with units of (3.0, 7.6, 33.5, 178, and 1000) $\times$ 10^{-9} photons s^{-1} cm^{-2} $arcsec^{-2}$. The final best-fit ellipse(s) are overlaid in green on both plots.

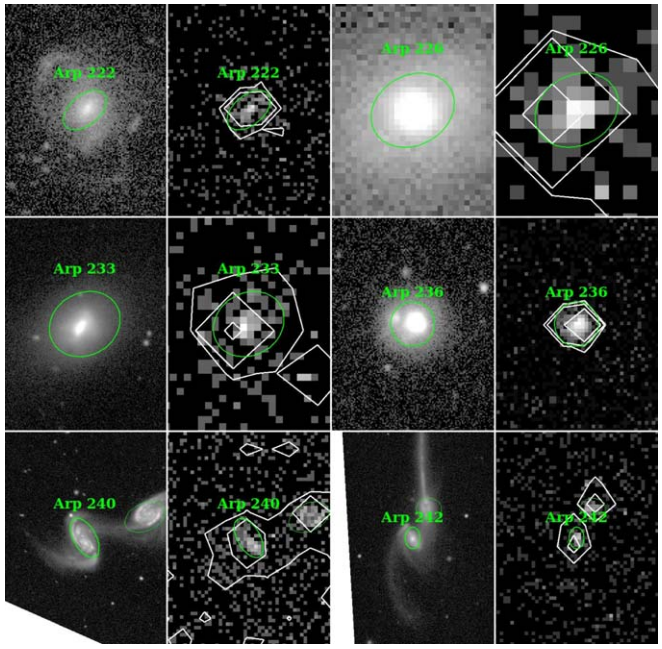

Figure 22. Montage of images of the galaxies. The left panel is either the SDSS g image or the *GALEX* NUV image (if no SDSS images exist). The right panel is the unsmoothed exposure-corrected *Chandra* 0.3–1.0 keV low-energy map. Logarithmic contours are overlaid in white on the *Chandra* image, with units of (3.0, 7.6, 33.5, 178, and 1000) $\times$ 10^{-9} photons s^{-1} cm^{-2} $arcsec^{-2}$. The final best-fit ellipse(s) are overlaid in green on both plots.

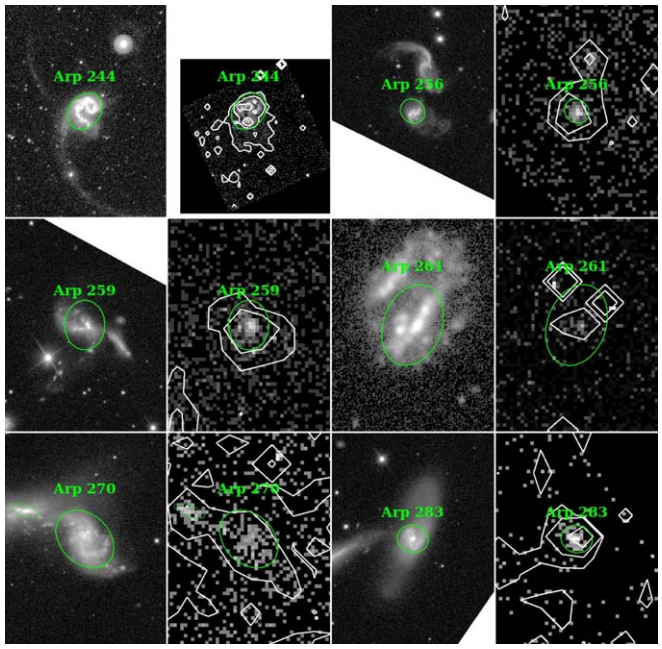

Figure 23. Montage of images of the galaxies. The left panel is either the SDSS g image or the *GALEX* NUV image (if no SDSS images exist). The right panel is the unsmoothed exposure-corrected *Chandra* 0.3–1.0 keV low-energy map. Logarithmic contours are overlaid in white on the *Chandra* image, with units of (3.0, 7.6, 33.5, 178, and 1000) $\times$ 10^{-9} photons s^{-1} cm^{-2} $arcsec^{-2}$. The final best-fit ellipse(s) are overlaid in green on both plots.

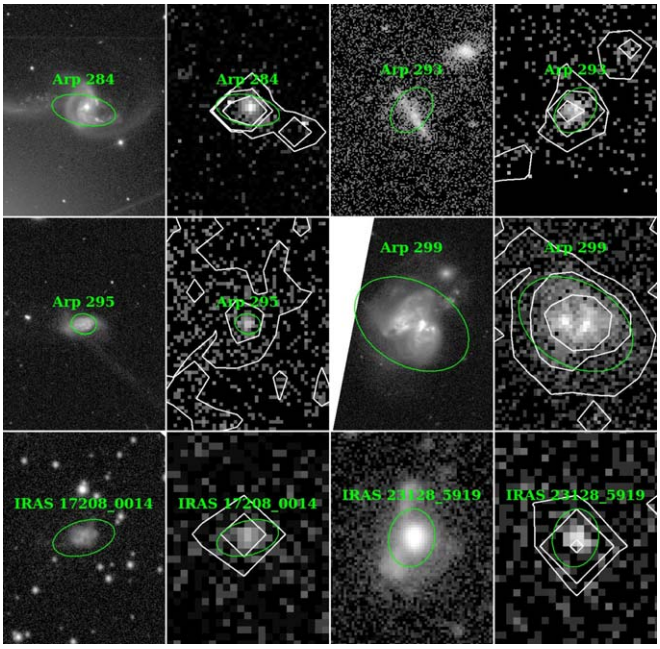

Figure 24. Montage of images of the galaxies. The left panel is either the SDSS g image or the *GALEX* NUV image (if no SDSS images exist). The right panel is the unsmoothed exposure-corrected *Chandra* 0.3–1.0 keV low-energy map. Logarithmic contours are overlaid in white on the *Chandra* image, with units of (3.0, 7.6, 33.5, 178, and 1000) $\times$ 10^{-9} photons s^{-1} cm^{-2} $arcsec^{-2}$. The final best-fit ellipse(s) are overlaid in green on both plots.

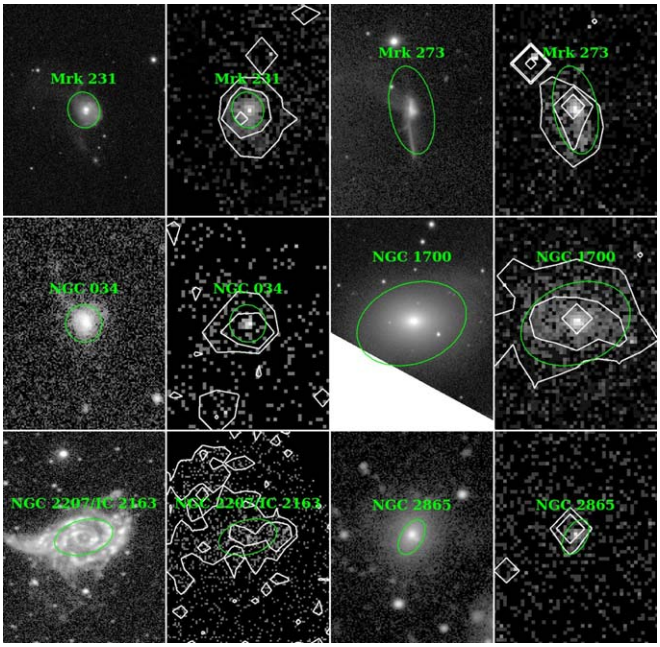

Figure 25. Montage of images of the galaxies. The left panel is either the SDSS g image or the *GALEX* NUV image (if no SDSS images exist). The right panel is the unsmoothed exposure-corrected *Chandra* 0.3–1.0 keV low-energy map. Logarithmic contours are overlaid in white on the *Chandra* image, with units of (3.0, 7.6, 33.5, 178, and 1000) $\times$ 10^{-9} photons s^{-1} cm^{-2} $arcsec^{-2}$. The final best-fit ellipse(s) are overlaid in green on both plots.

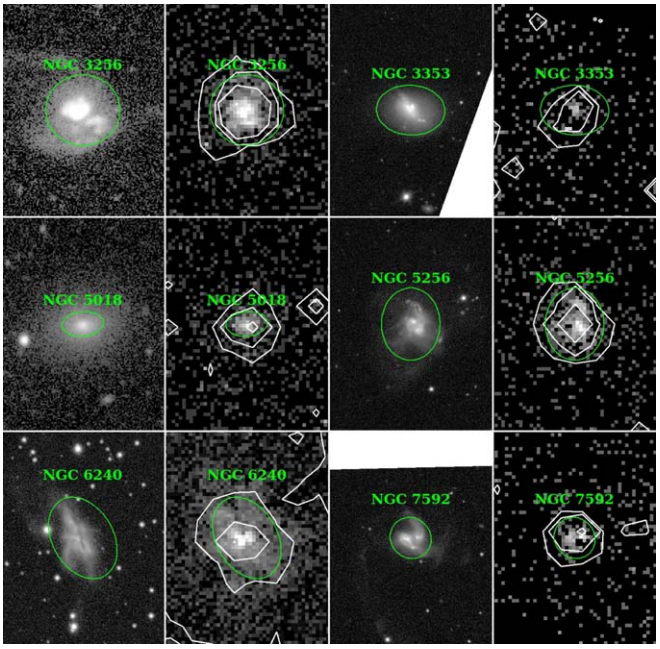

Figure 26. Montage of images of the galaxies. The left panel is either the SDSS g image or the *GALEX* NUV image (if no SDSS images exist). The right panel is the unsmoothed exposure-corrected *Chandra* 0.3–1.0 keV low-energy map. Logarithmic contours are overlaid in white on the *Chandra* image, with units of (3.0, 7.6, 33.5, 178, and 1000) $\times$ 10^{-9} photons s^{-1} cm^{-2} $arcsec^{-2}$. The final best-fit ellipse(s) are overlaid in green on both plots.

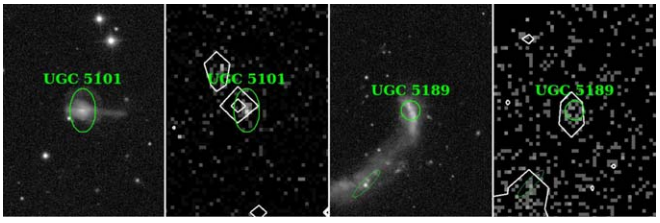

Figure 27. Montage of images of the galaxies. The left panel is either the SDSS g image or the *GALEX* NUV image (if no SDSS images exist). The right panel is the unsmoothed exposure-corrected *Chandra* 0.3–1.0 keV low-energy map. Logarithmic contours are overlaid in white on the *Chandra* image, with units of (3.0, 7.6, 33.5, 178, and 1000) $\times$ 10^{-9} photons s^{-1} cm^{-2} $arcsec^{-2}$. The final best-fit ellipse(s) are overlaid in green on both plots.

ORCID iDs

Beverly J. Smith https://orcid.org/0000-0002-8521-5240
Curtis Struck https://orcid.org/0000-0002-6490-2156
Roberto Soria https://orcid.org/0000-0002-4622-796X

References

Agertz, O., & Kravtsov, A. V. 2015, ApJ, 804, 18
Agertz, O., & Kravtsov, A. V. 2016, ApJ, 824, 79
Agertz, O., Kravtsov, A. V., Leitner, S. N., & Gnedin, N. Y. 2013, ApJ, 770, 25
Andreani, P., Boselli, A., Ciesla, L., et al. 2018, A&A, 617, 33
Arp, H. C. 1966, Atlas of Peculiar Galaxies (Pasadena, CA: Caltech)
Bell, E. F., & de Jong, R. S. 2000, ApJ, 550, 212

Bolatto, A. D., Wolfire, M., & Leroy, A. K. 2013, ARA&A, 51, 207
Boroson, B., Kim, D.-W., & Fabbiano, G. 2011, ApJ, 729, 12
Bournaud, F., Chapon, D., Teyssier, R., et al. 2011, ApJ, 730, 4
Brassington, N. J., Ponman, T. J., & Read, A. M. 2007, MNRAS, 337, 1439
Breitschwerdt, D., de Avillez, M. A., Feige, J., & Dettbarn, C. 2012, AN, 333, 486
Brinchmann, J., Charlot, S., White, S. D. M., et al. 2004, MNRAS, 351, 1151
Brook, C. B., Stinson, G., Gibson, B. K., Wadsley, J., & Quinn, T. 2012, MNRAS, 424, 1275
Brown, R. J. N., Forbes, D. A., Kissler-Patig, M., & Brodie, J. P. 2000, MNRAS, 317, 406
Brown, T., & Wilson, C. 2019, ApJ, 879, 17
Bushouse, H. A. 1987, ApJ, 320, 49
Bushouse, H. A., Lord, S. D., Lamb, S. A., Werner, M. W., & Lo, K. Y. 1999, arXiv:astro-ph/9911186
Bustard, C., Zweibel, E. G., & D'Onghia, E. 2016, ApJ, 819, 29
Casoli, F., Dupraz, C., Combes, F., & Kazes, I. 1991, A&A, 251, 1
Chevalier, R. A., & Clegg, A. W. 1985, Natur, 317, 44
Ciotti, L., D'Ecole, A., Pellegrini, S., & Renzini, A. 1991, ApJ, 376, 380
Ciotti, L., Pellegrini, S., Negri, A., & Ostriker, J. P. 2017, ApJ, 835, 15
Côté, S., Carignan, C., & Freeman, K. C. 2000, AJ, 120, 3027
Cox, A. L., & Sparke, L. S. 2004, AJ, 128, 2013
Cox, T. J., Jonsson, P., Primack, J. R., & Somerville, R. 2006, MNRAS, 373, 1013
Daddi, E., Elbaz, D., Walter, F., et al. 2010, ApJ, 714, L118
Dame, T. M., Hartmann, D., & Thaddeus, P. 2001, ApJ, 547, 792
Desert, F.-X., Boulanger, F., & Puget, J. L. 1990, A&A, 237, 215
Di Matteo, P., Bournaud, F., Martig, M., et al. 2008, A&A, 492, 31
Downes, D., & Solomon, P. M. 1998, ApJ, 507, 615
Doyle, M. T., Drinkwater, M. J., Rohde, D. J., et al. 2005, MNRAS, 361, 34
Elbaz, D., Arnaud, M., & Vangioni-Flam, E. 1995, A&A, 303, 345
Ellison, S. L., Patton, D. R., Simard, L., & McConnachie, A. W. 2008, ApJL, 672, L107
Elmegreen, B. G., Kaufman, M., Bournaud, F., et al. 2016, ApJ, 823, 26
English, J., Norris, R. P., Freeman, K. C., & Booth, R. S. 2003, AJ, 125, 1134
Fensch, J., Renaud, F., Bournaud, F., et al. 2017, MNRAS, 465, 1934
Fernández, X., Petric, A. O., Schweizer, F., & van Gorkom, J. H. 2014, AJ, 147, 74
Finlator, K., & Davé, R. 2008, MNRAS, 385, 2181
Gao, Y., & Solomon, P. M. 2004, ApJS, 152, 63
Gaspari, M., Eckert, D., Ettori, S., et al. 2019, arXiv:1904.10972
Georgakakis, A., Forbes, D. A., & Norris, R. P. 2000, MNRAS, 318, 124
Georgakakis, A., Hopkins, A. M., Caulton, A., et al. 2001, MNRAS, 326, 1431
Gordon, S., Koribalski, B., & Jones, K. 2001, MNRAS, 326, 578
Goulding, A., Greene, J. E., Ma, C.-P., et al. 2016, ApJ, 826, 167
Grimes, J. P., Heckman, T., Strickland, D., & Ptak, A. 2005, ApJ, 628, 187
Hayward, C. C., Torrey, P., Springel, V., Hernquist, L., & Vogelsberger, M. 2014, MNRAS, 442, 1992
Heckman, T. M., Alexandroff, R. M., Borthakur, S., Overzier, R., & Leitherer, C. 2015, ApJ, 809, 147
Hibbard, J. E., & van Gorkom, J. 1996, AJ, 111, 655
Hirschauer, A. S., Salzer, J. J., Janowiecki, S., & Wegner, G. A. 2018, AJ, 155, 82
Hopkins, P., Kereš, D., & Önorbe, J. 2014, MNRAS, 445, 581
Hopkins, P. F., Kereš, D., Norman, M., et al. 2013a, MNRAS, 433, 78
Hopkins, P. F., Narayanan, D., Murray, N., & Quataert, E. 2013b, MNRAS, 433, 69
Hopkins, P. F., Quataert, E., & Murray, N. 2011, MNRAS, 417, 950
Hopkins, P. F., Quataert, E., & Murray, N. 2012a, MNRAS, 421, 3522
Hopkins, P. F., Quataert, E., & Murray, N. 2012b, MNRAS, 421, 3488
Horellou, C., Casoli, F., Combes, F., & Dupraz, C. 1995, A&A, 298, 743
Houck, J. C., & Denicola, L. A. 2000, in ASP Conf. Proc. 216, Astronomical Data Analysis Software and Systems IX, ed. N. Manset, C. Veillet, & D. Crabtree (San Francisco, CA: ASP), 591
Huchtmeier, W. K., & Richter, O.-G. 1989, A General Catalog of HI Observations of Galaxies (New York: Springer)
Into, T., & Portinari, L. 2013, MNRAS, 430, 2715
Israel, F. P. 2005, A&A, 438, 8551
Izotov, Y. I., Guseva, N. G., Fricke, K. J., & Henkel, C. 2014, A&A, 561, A33
Izotov, Y. I., Guseva, N. G., Fricke, K. J., & Henkel, C. 2015, MNRAS, 451, 2251
Jo, Y.-S., Seon, K., Min, K.-W., et al. 2019, ApJS, 243, 9
Juneau, S., Narayanan, D. T., Moustakas, J., et al. 2009, ApJ, 707, 1217
Kennicutt, R. C., & Evans, N. J. 2012, ARA&A, 50, 531
Kennicutt, R. C., Jr. 1998, ARA&A, 36, 189
Kereš, D., Katz, N., Davé, R., Fardal, M., & Weinberg, D. H. 2009, MNRAS, 396, 2332
Kim, C.-G., & Ostriker, E. C. 2017, ApJ, 846, 133
Kim, D.-W., & Fabbiano, G. 2013, ApJ, 776, 116
Kleineberg, K., Sánchez-Blázquez, P., & Vazdekis, A. 2011, ApJ, 732, 33
Köppen, J., Weidner, C., & Kroupa, P. 2007, MNRAS, 375, 673
Kregenow, J. M., Sirk, M., Sankrit, R., et al. 2006, AAS, 209, 17.02
Lara-López, M. A., Cepa, J., Bongiovanni, A., et al. 2010, A&A, 521, 53
Larson, K., Sanders, D. B., Barnes, J. E., et al. 2016, ApJ, 825, 128
Li, J.-T., & Wang, Q. D. 2013, MNRAS, 435, 3071
Li, M., Ostriker, J. P., Cen, R., Bryan, G. L., & Naab, T. 2015, ApJ, 814, 4
Lotz, J. M., Jonsson, P., Cox, T. J., & Primack, J. R. 2000, MNRAS, 391, 1137
Ma, X., Hopkins, P. F., Faucher-Giguere, C.-A., et al. 2016, MNRAS, 456, 2140
Mannucci, F., Cresci, G., Maiolini, R., Marconi, A., & Gnerucci, A. 2010, MNRAS, 408, 2115
Maraston, C. 1998, MNRAS, 300, 872
Martin, J. M., Bottinelli, L., Dennefeld, M., & Gouguenheim, L. 1991, A&A, 245, 393
Mathews, W. G., & Brighenti, F. 2003, ARA&A, 41, 191
McCray, R. 1987, in Spectroscopy of Astrophysical Plasmas, ed. A. Dalgarno & D. Layzer (Cambridge: Cambridge Univ. Press), 255
McKee, C. F., & Cowie, L. L. 1977, ApJ, 215, 213
McQuinn, K. B. W., Skillman, E. D., Heilman, T. N., Mitchell, N. P., & Kelley, T. 2018, MNRAS, 477, 3164
Meiksin, A. 2016, MNRAS, 461, 2762
Mineo, S., Gilfanov, M., & Sunyaev, R. 2012b, MNRAS, 426, 1870
Mirabel, I. F., Booth, R. S., Garay, G., Johansson, L. E. B., & Sanders, D. B. 1990, A&A, 236, 327
Moreno, J., Torrey, P., Ellison, S. L., et al. 2019, MNRAS, 485, 1320
Muratov, A. L., Kereš, D., Faucher-Giguère, C.-A., et al. 2015, MNRAS, 454, 2691
Noeske, K. G., Weiner, B. J., Faber, S. M., et al. 2007, ApJL, 660, L43
Obreschkow, D., & Rawlings, S. 2009, MNRAS, 394, 1857
Orr, M. E., Hayward, C. C., Hopkins, P. F., et al. 2018, MNRAS, 478, 3653
O'Sullivan, E., Forbes, D. A., & Ponman, T. J. 2001, MNRAS, 328, 461
Owen, R. A., & Warwick, R. S. 2009, MNRAS, 394, 1741
Papadopoulos, P. P., van der Werf, P. P., Xilouris, E. M., et al. 2012, MNRAS, 426, 2601
Pellegrini, S., & Ciotti, L. 1998, A&A, 333, 433
Renaud, F., Bournaud, F., Agertz, O., et al. 2019, A&A, 625, 65
Renaud, F., Bournaud, F., Emsellem, E., et al. 2013, MNRAS, 436, 1836
Renaud, F., Bournaud, F., Emsellem, E., et al. 2015, MNRAS, 454, 3299
Renaud, F., Bournaud, F., Kraljic, K., & Duc, P.-A. 2014, MNRAS, 442, L33
Rieke, G. H., Lebofsky, M. J., Thompson, R. I., Low, F. J., & Tokunaga, A. T. 1980, ApJ, 238, 24
Sage, L. J., Salzer, J. J., Loose, H.-H., & Henkel, C. 1992, A&A, 265, 19
Sales, L. V., Navarro, J. F., Oman, K., et al. 2017, MNRAS, 464, 2419
Salim, S., Rich, R. M., Charlot, S., et al. 2007, ApJS, 173, 267
Sanders, D. B., & Mirabel, I. F. 1996, ARA&A, 34, 749
Sanders, D. B., Scoville, N. Z., & Soifer, B. T. 1991, ApJ, 370, 158
Schmidt, M. 1959, ApJ, 129, 243
Schweizer, F., & Seitzer, P. 1992, AJ, 104, 1039
Smith, B. J., Campbell, K., Struck, C., et al. 2018, AJ, 155, 81
Smith, B. J., Kleinmann, S. G., Huchra, J. P., & Low, F. J. 1987, ApJ, 318, 161
Smith, B. J., Struck, C., Hancock, M., et al. 2007, AJ, 133, 791
Smith, B. J., Swartz, D. A., Miller, O., et al. 2012, AJ, 142, 144
Smith, D. A., Herter, T., Haynes, M. P., Beichman, C. A., & Gautier, T. N. 1996, ApJS, 104, 217
Soifer, B. T., Sanders, D. B., Madore, B. F., et al. 1987, ApJ, 320, 238
Solomon, P. M., Downes, D., & Radford, S. J. E. 1992, ApJL, 387, L55
Solomon, P. M., Downes, D., Radford, S. J. E., & Barrett, J. W. 1997, ApJ, 478, 144
Sparre, M., & Springel, V. 2016a, MNRAS, 462, 2418
Springel, V. 2000, MNRAS, 312, 859
Statler, T. S., Smecker-Hane, T., & Cecil, G. N. 1996, AJ, 111, 1512
Strickland, D. K., Heckman, T. M., Colbert, E. J. M., Hoopes, C. G., & Weaver, K. A. 2004a, ApJS, 151, 193
Strickland, D. K., Heckman, T. M., Colbert, E. J. M., Hoopes, C. G., & Weaver, K. A. 2004b, ApJ, 606, 829
Strickland, D. K., Heckman, T. M., Weaver, K. A., & Dahlem, M. 2000, AJ, 120, 2965
Strickland, D. K., & Stevens, I. R. 2000, MNRAS, 314, 511
Su, Y., Irwin, J. A., White, R. E., & Cooper, M. C. 2015, ApJ, 806, 156
Teyssier, R., Chapon, D., & Bournaud, F. 2010, ApJL, 720, L149

Torres-Flores, S., Epinat, B., Amram, P., Plana, H., & Mendes de Olivera, C. 2011, MNRAS, 416, 1936
Torrey, P., Vogelberger, M., Marinacci, F., et al. 2019, MNRAS, 484, 5587
Trujillo-Gomez, S., Klypin, A., Colín, P., et al. 2015, MNRAS, 446, 1140
Ueda, J., Iono, D., Yun, M. S., et al. 2014, ApJS, 214, 29
van de Voort, F., Quataert, E., Hopkins, P. F., et al. 2016, MNRAS, 463, 4533
van den Bosch, F. C. 2000, ApJ, 530, 177
van Driel, W., Arnaboldi, M., Combes, F., & Sparke, L. S. 2000, A&AS, 141, 385
Weider, C., Ferraras, I., Vazdekis, A., & La Barbera, F. 2013, MNRAS, 435, 2274
Wiklind, T., Combes, F., & Henkel, C. 1995, A&A, 297, 643
Wu, J., Evans, N. J., II, Shirley, Y. L., & Knez, C. 2010, ApJS, 188, 313
Young, J. S., Allen, L., Kenney, J. D. P., Lesser, A., & Rownd, B. 1996, AJ, 112, 1903
Young, J. S., Kenney, J. D., Tacconi, L., et al. 1986, ApJL, 311, L17
Zhang, D., Thompson, T. A., Murray, N., & Quataert, E. 2014, ApJ, 784, 93
Zhu, M., Seaquist, E. R., Davoust, E., Frayer, D. T., & Bushouse, H. A. 1999, AJ, 118, 145